



**HAL**  
open science

## **A phenomenological model of soil evaporative efficiency using surface soil moisture and temperature data**

Olivier Merlin, Luis Enrique Olivera-Guerra, Bouchra Aït Hssaine, Abdelhakim Amazirh, Zoubair Rafi, Jamal Ezzahar, Pierre Gentine, Said Khabba, Simon Gascoin, Salah Er-Raki

### ► **To cite this version:**

Olivier Merlin, Luis Enrique Olivera-Guerra, Bouchra Aït Hssaine, Abdelhakim Amazirh, Zoubair Rafi, et al. A phenomenological model of soil evaporative efficiency using surface soil moisture and temperature data. *Agricultural and Forest Meteorology*, 2018, 256-257, pp.501 - 515. 10.1016/j.agrformet.2018.04.010 . hal-01912436

**HAL Id: hal-01912436**

**<https://hal.science/hal-01912436>**

Submitted on 5 Nov 2018

**HAL** is a multi-disciplinary open access archive for the deposit and dissemination of scientific research documents, whether they are published or not. The documents may come from teaching and research institutions in France or abroad, or from public or private research centers.

L'archive ouverte pluridisciplinaire **HAL**, est destinée au dépôt et à la diffusion de documents scientifiques de niveau recherche, publiés ou non, émanant des établissements d'enseignement et de recherche français ou étrangers, des laboratoires publics ou privés.

# A phenomenological model of soil evaporative efficiency using surface soil moisture and temperature data

Olivier Merlin<sup>\*,a,b</sup>, Luis Olivera-Guerra<sup>a</sup>, Bouchra Aït Hssaine<sup>a,b</sup>,  
Abdelhakim Amazirh<sup>a,b</sup>, Zoubair Rafi<sup>a,b</sup>, Jamal Ezzahar<sup>b</sup>, Pierre Gentine<sup>c</sup>,  
Said Khabba<sup>b</sup>, Simon Gascoin<sup>a</sup>, Salah Er-Raki<sup>b</sup>

<sup>a</sup>*CESBIO, Université de Toulouse, IRD/UPS/CNRS/CNES, Toulouse, France*

<sup>b</sup>*Cadi Ayyad University, Marrakech, Morocco*

<sup>c</sup>*Columbia University, New York, USA*

---

## Abstract

Modeling soil evaporation has been a notorious challenge due to the complexity of the phenomenon and the lack of data to constrain it. In this context, a parsimonious model is developed to estimate soil evaporative efficiency (SEE) defined as the ratio of actual to potential soil evaporation. It uses a soil resistance driven by surface (0 – 5 cm) soil moisture, meteorological forcing and time (hour) of day, and has the capability to be calibrated using the radiometric surface temperature derived from remotely sensed thermal data. The new approach is tested over a rainfed semi-arid site, which had been under bare soil conditions during a 9-month period in 2016. Three calibration strategies are adopted based on SEE time series derived from 1) eddy-covariance measurements, 2) thermal measurements, and 3) eddy-covariance measurements used only over separate drying periods between significant rainfall events. The correlation coefficients (and slopes of the linear regression) between simulated and observed (eddy-covariance-derived) SEE

---

\*email: [olivier.merlin@cesbio.cnes.fr](mailto:olivier.merlin@cesbio.cnes.fr)

are 0.85, 0.86 and 0.87 (and 0.91, 0.87 and 0.91) for calibration strategies 1, 2 and 3, respectively. Moreover, the correlation coefficient (and slope of the linear regression) between simulated and observed SEE is improved from 0.80 to 0.85 (from 0.86 to 0.91) when including hour of day in the soil resistance. The reason is that, under non-energy-limited conditions, the receding evaporation front during daytime makes SEE decrease at the hourly time scale. The soil resistance formulation can be integrated into state-of-the-art dual-source surface models and has calibration capabilities across a range of spatial scales from spaceborne microwave and thermal data.

*Key words:* Soil evaporation, soil resistance, soil moisture, surface temperature, calibration, remote sensing.

---

## 1. Introduction

To better understanding the water fluxes of crops, and optimizing irrigation in water-limited environments, efforts are being made to estimate both the plant consumption by transpiration (through stomata) and the water losses by evaporation (from soil and in some instances from canopy via interception) (Agam et al., 2012). The partitioning of evapotranspiration into soil evaporation and plant transpiration is needed to assess the crop water use efficiency through its transpiration rate (Hain et al., 2009), as well as to evaluate how much production is derived per unit of crop transpiration (Molden et al., 2010). Such information is also needed at multiple spatial scales, from the field scale where agronomic practices are carried out (Allen, 1990), to the catchment scale where land and water management is operated (Zhang et al., 2001).

14 Field instrumentation for measuring soil evaporation and plant transpi-  
15 ration separately includes eddy covariance, micro Bowen-ratio energy bal-  
16 ance, micro lysimeter, soil heat pulse probe, chamber, isotope and sap flow  
17 techniques (Kool et al., 2014). Although those instrumentations have much  
18 evolved since the initial experimentations in the 1970s, data collected *in*  
19 *situ* are still very scarce (Schlesinger and Jasechko, 2014) and are generally  
20 representative of the local conditions, that is from the leaf/stem to approxi-  
21 mately the 100-m scale. This results in a large uncertainty of the transpira-  
22 tion/evapotranspiration ratio (estimated in the range 0.35 – 0.80) associated  
23 with a current lack of observation at the catchment scale (Coenders-Gerrits  
24 et al., 2014).

25 To help evaluate the evaporation/transpiration partitioning at multiple  
26 space-time scales, advanced land-surface models are available to simulate en-  
27 ergy, water, and carbon fluxes at the land surface-atmosphere interface (Ole-  
28 son et al., 2013; Boone et al., 2017, e.g.). Simpler models such as two-source  
29 surface energy balance models (Lhomme and Chehbouni, 1999) require less  
30 input parameters. In general, state-of-the-art models rely on specific assump-  
31 tions on either the soil evaporation (Caparrini et al., 2004) or the plant tran-  
32 spiration (Kustas and Norman, 1999), or base their two-source representation  
33 on semi-empirical or semi-physical resistances. Whereas semi-empirical resis-  
34 tances are difficult to generalize in a range of agro-environmental conditions  
35 (Ershadi et al., 2014), semi-physical resistances generally depend on soil hy-  
36 drodynamic properties (Decker et al., 2017), which are highly variable and  
37 yet unavailable over large areas (Gutmann and Small, 2007).

38 To address the above-described difficulties in representing the evapora-

39 tion/transpiration components across a range of space-time scales using a  
40 two-source resistance-based formulation, remote sensing data have great po-  
41 tential. In fact, one way of separating soil evaporation and plant transpiration  
42 is to estimate one component independently from the total evapotranspira-  
43 tion. In this regard, the soil evaporation process is quite well constrained  
44 by available remote sensing observations. Surface soil moisture derived from  
45 microwave data is one main controlling factor of evaporation (Prévot et al.,  
46 1984), and the radiometric soil temperature derived from thermal data in  
47 the absence of dense vegetation cover is, under non-energy-limited condi-  
48 tions, a signature of the evaporation rate (Norman et al., 1995). However,  
49 although thermal-microwave data combining approaches have been imagined  
50 since the 1990s (Chanzy et al., 1995; Li et al., 2006), none has been imple-  
51 mented yet. One of the reasons is the lack of remote sensing sensors with  
52 sufficient spatio-temporal resolution. Especially, the operational extraction  
53 of surface soil moisture at high-spatial resolution remains delicate and there  
54 is no thermal mission providing data at high spatio-temporal resolution. As  
55 a step forward, recently launched/future satellite missions such as Sentinel-1  
56 (Paloscia et al., 2013) and Trishna (Lagouarde et al., 2013) as well as disag-  
57 gregation techniques (Peng et al., 2017; Zhan et al., 2013) could solve this  
58 issue in the near future.

59 Another major issue when attempting to integrate thermal data in an  
60 evaporation model is the drying (usually around noon) of the top few mil-  
61 limeters of soil which inhibits evaporation, regardless of the availability of the  
62 soil water underneath (Mahrt and Pan, 1984; Dickinson et al., 1986; Soares  
63 et al., 1988; Wetzzel and Chang, 1988; Van de Griend and Owe, 1994; Heitman

64 et al., 2008; Shahraeeni et al., 2012). Or et al. (2013) identify two regimes:  
65 Stage I when both liquid phase continuity and capillary forces sustain evap-  
66 oration at the top soil and Stage II when the drying front is deeper in the  
67 soil and evaporation is mainly controlled by diffusion (Haghighi et al., 2013).  
68 In fact, the soil drying during daytime and the uniform rewetting of soil via  
69 capillary rises during nighttime is a cyclic phenomenon that is expected to  
70 affect the evaporation resistance at the hourly time scale (Tuzet et al., 2003).  
71 One challenge is that the radiometric soil temperature is highly variable in  
72 time as a result of the diurnal dynamics of meteorological forcing (i.e. solar  
73 radiation, wind speed, air temperature, air humidity) and the evolution of  
74 soil moisture. Additionally, it is representative of the physical characteristics  
75 of the soil skin only. A direct consequence is that a thermal-based evapo-  
76 ration model should beneficially take into account the drying of the top soil  
77 during daytime.

78 This was the rationale for developing a formulation of soil evaporative  
79 efficiency (SEE, defined as the ratio of actual to potential soil evaporation)  
80 with a shape that adapts to the soil moisture gradient. Given that the soil  
81 moisture profile is generally unknown, and that the drying of the top soil is  
82 related to the evaporative demand (in addition to the soil moisture value),  
83 Merlin et al. (2011) considered potential evaporation as a proxy for the soil  
84 moisture gradient in the topsoil. In fact, a large potential evaporation is  
85 associated with a strong moisture gradient in the top soil, which implies  
86 a decrease of SEE regardless of the moisture content integrated over the  
87 0 – 5 cm soil layer. Such a phenomenological modeling approach allows for  
88 implicitly representing the drying of the top soil during daytime. The SEE

89 formulation of Merlin et al. (2011) was derived at the daily scale only, which  
90 is inconsistent with the subdiurnal availability of thermal data.

91 In this context, this paper aims to develop a quasi instantaneous model  
92 of SEE that has the ability to consistently integrate both near-surface soil  
93 moisture and radiometric soil temperature data. In practice, the recent SEE  
94 modeling approach of Merlin et al. (2016) is improved by adding a temporal  
95 dependence, as well as an additional parameter controlling the cyclic phe-  
96 nomenon of the drying/rewetting of the top soil during daytime/nighttime.  
97 The new resistance model is tested in terms of SEE estimates using eddy  
98 covariance measurements collected over a bare soil site in central Morocco,  
99 and its performance is assessed against two benchmark models. Calibration  
100 capabilities of the SEE model from thermal (instead of eddy covariance) data  
101 are also investigated.

## 102 2. Modeling approach

103 Soil evaporation can be modeled using a resistance approach:

$$LE = \frac{\rho C_P}{\gamma} \times \frac{e_{sat}(T) - e_a}{r_{ah} + r_{ss}} \quad (1)$$

104 with  $LE$  ( $\text{W m}^{-2}$ ) being the soil latent heat flux,  $r_{ss}$  ( $\text{s m}^{-1}$ ) the resistance  
105 to the diffusion of vapor in soil pores,  $\rho$  ( $\text{kg m}^{-3}$ ) the density of air,  $C_P$  ( $\text{J}$   
106  $\text{kg}^{-1} \text{K}^{-1}$ ) the specific heat capacity of air,  $\gamma$  ( $\text{Pa K}^{-1}$ ) the psychrometric  
107 constant,  $e_{sat}(T)$  (Pa) the saturated vapor pressure at the soil surface,  $T$  (K)  
108 the soil surface temperature,  $e_a$  (Pa) the vapor pressure of air and  $r_{ah}$  ( $\text{s}$   
109  $\text{m}^{-1}$ ) the aerodynamic resistance to heat transfer from the soil surface to the  
110 reference height.

111 Based on Equation (1), one may also derive a potential soil evaporation,  
 112 defined as the soil evaporation that would occur in fully saturated soil con-  
 113 ditions so that  $r_{ss} = 0$ :

$$LEp = \frac{\rho C_P}{\gamma} \times \frac{e_{sat}(T_{wet}) - e_a}{r_{ah,wet}} \quad (2)$$

114 with  $T_{wet}$  (K) and  $r_{ah,wet}$  ( $s\ m^{-1}$ ) being the soil temperature and aerodynamic  
 115 resistance in saturated soil conditions, respectively. The parameters used as  
 116 input to the  $LEp$  model are presented in the Appendix A. The ratio of actual  
 117 to potential soil evaporation, i.e. the SEE, can then be expressed as:

$$SEE = \frac{e_{sat}(T) - e_a}{e_{sat}(T_{wet}) - e_a} \times \frac{r_{ah,wet}}{r_{ah} + r_{ss}} \quad (3)$$

118 The soil resistance in Equation (3) is expressed as a function of soil mois-  
 119 ture following Merlin et al. (2016):

$$r_{ss,M16} = r_{ss,ref} \exp(-\theta/\theta_{efolding}) \quad (4)$$

120 with  $r_{ss,ref}$  being a hypothetical soil resistance corresponding to dry soil con-  
 121 ditions and  $\theta_{efolding}$  the soil moisture value at which  $r_{ss}$  is equal to  $r_{ss,ref}/e$ .  
 122 The present paper aims to intercompare three evaporation models based on  
 123 the following assumptions for the  $r_{ss}$  formulation:

- 124 • both  $r_{ss,ref}$  and  $\theta_{efolding}$  of Equation (4) are set to constant values  
 125 (depending on soil texture and structure) as in Passerat de Silans (1986)  
 126 and Sellers et al. (1992).
- 127 •  $r_{ss,ref}$  and  $\theta_{efolding}$  of Equation (4) are analytically expressed as a func-  
 128 tion of meteorological forcing and two observable parameters as in Mer-  
 129 lin et al. (2016).

130 • a correction term ( $\delta r_{ss,t}$ ) is added to  $r_{ss,M16}$  to account for diurnal  
 131 variations in SEE associated with top-soil drying (receding evaporation  
 132 front) during daytime (Mahrt and Pan, 1984; Dickinson et al., 1986;  
 133 Soarès et al., 1988; Wetzels and Chang, 1988; Van de Griend and Owe,  
 134 1994; Heitman et al., 2008; Shahraeeni et al., 2012).

135 For clarity, the three above models are named in the following as PdS86,  
 136 M16 and new model, respectively.

137 The third and new soil resistance model is written as:

$$r_{ss,t} = r_{ss,M16} + \delta r_{ss,t} \quad (5)$$

138 with  $r_{ss,M16}$  the soil resistance of Equation (4) and  $\delta r_{ss,t}$  a correction term  
 139 that includes the effect of the receding evaporation front during daytime on  
 140 quasi-instantaneous SEE. A phenomenological expression of  $\delta r_{ss,t}$  is proposed  
 141 below as a function of time of day centered at solar noon ( $\delta t = t - 12$  with  
 142  $t$  in unit of hour). The SEE difference between time  $t$  and 12 pm ( $\delta SEE_t$ )  
 143 can be expressed as:

$$SEE_t = SEE_{12} + \delta SEE_t \quad (6)$$

144 Now, we assume (this assumption will be shown to be valid in section 4) that  
 145 the relative diurnal variations in SEE are linearly dependent on the time of  
 146 day  $\delta t$ :

$$\delta SEE_t = -SEE_{12} \times \delta t / \tau_{hyst} \quad (7)$$

147 with  $\tau_{hyst}$  being a parameter (unit of hour) that characterizes the hysteretic  
 148 time scale associated with the evaporative front drying during daytime, and  
 149 the uniform rewetting of soil via capillary rises during nighttime. A rela-  
 150 tionship between  $\delta SEE_t$  and  $\delta r_{ss,t}$  is then built through the derivative of

151 Equation (3):

$$\delta SEE_t = -\frac{SEE_{12}}{r_{ah,12} + r_{ss,12}} \times \delta r_{ss,t} \quad (8)$$

152 with  $r_{ss,12}$  and  $r_{ah,12}$  being the soil and aerodynamic resistance estimated at  
153 noon, respectively. Herein,  $r_{ss,12}$  is approximated by the M16 soil resistance  
154 (noted  $r_{ss,M16}$ ) by assuming that  $\theta$  does not vary much at the subhourly time  
155 scale (a reasonable assumption), and  $r_{ah,12}$  is approximated by  $r_{ah}$  at time  $t$ ,  
156 so that  $\delta r_{ss,t}$  can be instantly (not recursively) computed regardless of the  
157 conditions at noon. Hence, by substituting  $\delta SEE_t$  in the above equation,  
158 one obtains:

$$\delta r_{ss,t} = (r_{ah} + r_{ss,M16}) \times \delta t / \tau_{hyst} \quad (9)$$

### 159 **3. Data**

#### 160 *3.1. Sidi Rahal site*

161 The Sidi Rahal site (-7.3535 E; 31.7035 N) is located east of the Tensift  
162 basin in central Morocco (see Figure 1). The climate is semi-arid with an  
163 annual precipitation of about 250 mm mostly concentrated between Novem-  
164 ber and April and a reference crop evapotranspiration of 1600 mm per year.  
165 The Sidi Rahal monitoring station was set up in a rainfed wheat field in De-  
166 cember 2013 in the framework of a joint international project (Khabba et al.,  
167 2013; Jarlan et al., 2015). Due to an unusual lack of precipitation late 2015,  
168 the winter wheat crop had not been planted during the 2015-2016 season.  
169 As a result, the crop field remained in bare soil conditions from January to  
170 September 2016, which we took advantage of to test evaporation models in  
171 ideal conditions. The soil texture is predominantly loam.

172 The station is equipped with an eddy-covariance (EC) system, radiome-  
173 ters operating in the short and long wavelengths, heat flux plates and soil  
174 moisture probes. The net radiation is measured by a Kipp & Zonen CNR1.  
175 The soil heat flux is estimated with Hukseflux HFP-01 plates buried at 5  
176 cm depth. Those data are collected with a time step of 10 s and then av-  
177 eraged and recorded every 30 minutes. Latent and sensible heat fluxes are  
178 estimated with a Campbell Scientific KH20 fast response hygrometer and a  
179 Campbell Scientific CSAT3 anemometer at a frequency of 10 Hz and then  
180 converted to a 30-minute average. Both latent and sensible heat fluxes are  
181 corrected for energy balance lack of closure using the Bowen ratio method.  
182 The daily (computed using 30-minute estimates between 9 am and 5 pm)  
183 Bowen ratio and the 30-minute flux estimates are combined to derive the  
184 corrected 30-minute latent and sensible heat fluxes. The 5-cm soil moisture  
185 is measured by a Campbell Scientific CS616 calibrated using periodic gravi-  
186 metric measurements. The radiometric surface temperature is derived from  
187 an Apogee instruments 8-14  $\mu\text{m}$  thermal infrared (TI) radiometer set up at a  
188 2-m height. Meteorological forcing data including air temperature, solar radi-  
189 ation, relative humidity, wind speed and rainfall are monitored continuously  
190 at a semihourly time step at 2 m as well.

### 191 *3.2. SEE estimates*

192 Given the bare soil conditions of the Sidi Rahal site during the study pe-  
193 riod, evapotranspiration originates only from soil in this experiment. There-  
194 fore, evapotranspiration and soil evaporation, as well as potential evapotran-  
195 spiration and potential soil evaporation, are assumed to be the same. An  
196 estimate of SEE can hence be obtained by dividing the measured latent heat

197 flux by potential (soil) evaporation:

$$SEE_{EC} = \frac{LE_{EC}}{LEp} \quad (10)$$

198 with  $SEE_{EC}$  being the EC-derived SEE,  $LE_{EC}$  the evaporation measured by  
199 EC and  $LEp$  the evaporation in saturated soil conditions (Equation 2).

200 Another relatively independent, indirect, estimate of SEE is derived from  
201 the radiometric soil temperature:

$$SEE_{TI} = \frac{T_{dry} - T_{TI}}{T_{dry} - T_{wet}} \quad (11)$$

202 with  $SEE_{TI}$  the TI-derived SEE,  $T_{TI}$  the surface soil temperature retrieved  
203 from TI measurements, and  $T_{dry}$  and  $T_{wet}$  the soil temperature in bone-dry  
204 and saturated soil conditions, respectively (Merlin, 2013; Stefan et al., 2015).

205 In practice,  $T_{dry}$  and  $T_{wet}$  (together with  $LEp$ ) are simulated by the same  
206 soil energy balance model by setting  $r_{ss} = \infty$  and  $r_{ss} = 0$  in Equation  
207 (1), respectively. The reader is advised to refer to Appendix A for more  
208 information on the energy balance model.

209 Figure 2 plots the half-hourly surface soil moisture and EC- and TI-  
210 derived SEE (for data collected between 6 am and 6 pm with  $LEp > 100$   
211  $\text{Wm}^{-2}$ ) as a function of day of year (DOY) 1 to 243 in 2016. One observes  
212 a strong correlation between SEE estimates and  $\theta$ , as all drying periods are  
213 visible in the SEE time series. However, the TI-derived SEE is more scat-  
214 tered than the EC-derived SEE. As mentioned above, one major objective  
215 of this study is to assess the calibration capabilities of a SEE model using  
216 consistent but uncertain TI-derived estimates. A total of 9 study periods are  
217 defined for calibration and validation purposes: the whole study period noted  
218  $P0$  (DOY 1 – 243) and 8 subperiods  $P1 - 8$  bounded by significant rainfall

219 events. The start and end DOY of each subperiod  $P_i$  for  $i = 1, \dots, 8$  are  
 220 listed in Table 1. Note that many points corresponding to TI measurements  
 221 exhibit a SEE larger than 1 or smaller than 0 in Figure 2. It means that  
 222 the modeled  $T_{dry}$  and  $T_{wet}$  can be smaller and larger than the observed tem-  
 223 perature, respectively. This may be due to several factors: uncertainties in  
 224 thermal data, uncertainties in modeled  $T_{wet}$  and  $T_{dry}$ , and/or uncertainties in  
 225 the model linking SEE to soil temperature.  $SEE_{TI}$  values larger than 1 and  
 226 smaller than 0 mostly correspond to the early (before noon) and late (after  
 227 noon) hours of dates with very wet and very dry conditions, respectively.

228 Figure 3 illustrates the variations during daytime of potential soil evapora-  
 229 tion, the soil evaporation measured by the EC system and the soil evaporation  
 230 derived as TI-derived SEE times potential evaporation for a relatively wet  
 231 ( $\theta \sim 0.18 \text{ m}^3\text{m}^{-3}$ ) and dry ( $\theta \sim 0.05 \text{ m}^3\text{m}^{-3}$ ) day separately. Both EC- and  
 232 TI-derived estimates are rather close, especially at around 12 pm. However,  
 233 the time at which the maximum LE value is reached is about 11:00-11:30  
 234 am for TI-derived estimates, 12:15-12:45 pm for EC-derived estimates and  
 235 1:15-1:30 pm for potential evaporation. Differences in the time of maximum  
 236 latent heat flux value can be interpreted as the impact of top-soil drying i.e.  
 237 the downward-moving drying front that counters the evaporation process (Or  
 238 et al., 2013). The maximum of  $LE_{EC}$  logically appears sooner than that of  
 239  $LE_p$ , due to the decrease of soil evaporation associated with the receding  
 240 of evaporation front in the top soil at around noon. Such phenomenon is  
 241 visible in both relatively wet and dry conditions as illustrated in Figure 3.  
 242 The fact that the maximum of  $SEE_{TI} \times LE_p$  appears sooner than that of  
 243  $LE_{EC}$  is explained by the difference in the depth (within the top 0 – 5 cm

244 layer) at which the actual soil evaporation occurs and that (near-surface) of  
245 TI data. Hence, the thinner the soil layer used to represent evaporation, the  
246 more sensitive the evaporation model is to the daytime top-soil drying.

247 Figure 3 also presents the hysteretic behavior of radiometric temperature  
248 as a function of  $LEp$ . For a given level of  $LEp$ , the surface soil is cooler in the  
249 morning than in the afternoon, explaining the decreasing rate of TI-derived  
250 evaporation ( $SEE_{TI} \times LEp$ ) during daytime. Note that the simulated ex-  
251 treme temperatures  $T_{dry}$  and  $T_{wet}$  do not follow the same hysteretic behavior,  
252 as similar values are obtained (for  $LEp > 200 \text{ Wm}^{-2}$ ) before and after the  
253 time of  $LEp$  maximum value. Hysteresis effects are nill in dry conditions  
254 because when the soil is completely dry, evaporation stops. Hysteresis effects  
255 are also theoretically nill in fully wet conditions, because when the soil is  
256 maintained permanently wet, evaporation is at its potential rate at any time  
257 of day. Another interesting feature of the temporal signature of radiometric  
258 temperature is its link with wind speed. Whereas the increase of the drying  
259 front intrusion during the day makes  $T$  increase, an increase in wind speed  
260 has instead the effect of decreasing  $T$  (increasing  $SEE_{TI}$ ) due to the drop  
261 in  $r_{ah}$ . Nonetheless, extreme temperatures  $T_{wet}$  and  $T_{dry}$  are estimated using  
262 quasi instantaneous wind speed as input to the energy balance model, and  
263 therefore, the TI-derived SEE is less influenced by wind speed than the un-  
264 normalized  $T$ . For instance, the correlation coefficient between unnormalized  
265  $T$  and wind speed is 0.85 (0.69) for the wet (dry) date of Figure 3 while it is  
266  $-0.03$  ( $-0.06$ ) between normalized  $T$  and wind speed, respectively.

## 267 4. Calibration strategies

268 Various calibration strategies of M16 (Equation 4) and the new  $r_{ss}$  model  
269 (Equation 5) are investigated depending on the nature of SEE estimates  
270 (derived either from EC or TI data) and on the length of observed SEE time  
271 series.

### 272 4.1. Calibrating $r_{ss,ref}$ and $\theta_{efolding}$

273 In Merlin et al. (2016), the  $r_{ss,ref}$  and  $\theta_{efolding}$  parameters of Equation  
274 (4) are analytically expressed as a function of meteorological forcing, cut-  
275 off soil moisture value  $\theta_{1/2}$  at which  $SEE=0.5$  and first derivative of SEE  
276 at  $\theta_{1/2}$ , named  $\Delta\theta_{1/2}^{-1}$ . The main equations are reminded in Appendix B.  
277 In fact, both parameters  $\theta_{1/2}$  and  $\Delta\theta_{1/2}^{-1}$  are estimated directly from a time  
278 series of SEE and  $\theta$  observations. Merlin et al. (2016) developed a specific  
279 calibration approach to take into account the non-linearity of the  $SEE(\theta)$   
280 relationship, as well as to adapt for data sets with soil moisture values that  
281 may not be uniformly distributed around the targeted  $\theta_{1/2}$  value. In the  
282 same way as in Merlin et al. (2016), the full SEE range  $[0 - 1]$  is split into  
283 20 (0.05-wide) bins, and the SEE and  $\theta$  values falling into each SEE bin are  
284 averaged separately to provide a pair  $(SEE_k, \theta_k)$  per bin. Then, 10 segments  
285 are computed by joining the two points  $(SEE_k, \theta_k)$  and  $(SEE_{k+10}, \theta_{k+10})$  for  
286  $k = 1, \dots, 10$ . Nevertheless, an improvement is made herein to 1) estimate the  
287 pair  $(\theta_{1/2}, \Delta\theta_{1/2}^{-1})_k$  for each segment  $k$  and 2) weight the pair  $(\theta_{1/2}, \Delta\theta_{1/2}^{-1})_k$   
288 according to the mean difference between the ordinate of the center of the  
289 segment  $k$  and 0.5. In practice, we define the weight  $w_k$  such as: i)  $w_k = 1$   
290 for  $\overline{SEE}_k = 0.5$  and ii)  $w_k = 0$  for  $\overline{SEE}_k = 0.25$  or  $\overline{SEE}_k = 0.75$ , with

291  $\overline{SEE}_k = (SEE_k + SEE_{k+10})/2$ . A general equation of  $w_k$  is obtained by  
 292 considering a linear interpolation between extreme values:

$$w_k = 1 - 4 \times |0.5 - \overline{SEE}_k| \quad (12)$$

293 Note that the values allocated for the weighting function correspond to the  
 294 simplest (triangular) function with a weight set to 0 and 1 for the extreme  
 295 (one end point of a segment is associated to  $SEE \sim 0$  or  $SEE \sim 1$ ) and  
 296 middle (mean  $SEE = 0.5$ ) case, respectively. The new calibration procedure  
 297 aims to give a larger weight to the segments that are close to the inflexion  
 298 point of the  $SEE(\theta)$  relationship and a smaller weight to the segments that  
 299 are located in a region where the nonlinearity of the  $SEE(\theta)$  relationship is  
 300 more prominent. The quasi linearity of the  $SEE(\theta)$  relationship around  $\theta_{1/2}$   
 301 is indeed an assumption of the above calibration strategy.

302 By way of illustration, Figure 4 plots EC-derived SEE versus  $\theta$  and TI-  
 303 derived SEE versus  $\theta$  for data with  $LEp > 400 \text{ Wm}^{-2}$  (arbitrary threshold)  
 304 during the whole time period  $P0$ . **Such a threshold is chosen to separate**  
 305 **between relatively low and high  $LEp$  conditions.** The above described cal-  
 306 ibration procedure of  $(\theta_{1/2}, \Delta\theta_{1/2}^{-1})$  is applied to both time series separately.  
 307 Although the TI-derived SEE values appear to be more scattered than the  
 308 EC-derived SEE, calibrated parameters have similar values in both cases:  $\theta_{1/2}$   
 309 is 0.129 and 0.125  $\text{m}^3\text{m}^{-3}$ , and  $\Delta\theta_{1/2}^{-1}$  is 4.01 and 4.21  $\text{m}^3\text{m}^{-3}$  for EC and TI  
 310 case, respectively. Note that  $\theta_{1/2}$  and  $\Delta\theta_{1/2}^{-1}$  may vary with parameters other  
 311 than  $\theta$  and texture (Merlin et al., 2016). For instance, the work in Chanzy  
 312 and Bruckler (1993), a theoretical analysis supported by experimental evi-  
 313 dences, has shown the role of  $LEp$  and wind velocity in the determination  
 314 of  $\theta_{1/2}$ . Therefore, applying the calibration approach over several shorter

315 periods  $P1 - 8$  may help improving model performances.

316 Once  $\theta_{1/2}$  and  $\Delta\theta_{1/2}^{-1}$  values have been retrieved, two different strategies  
317 are investigated to estimate  $r_{ss,ref}$  and  $\theta_{efolding}$  parameters of Equation (4):

- 318 • For M16,  $r_{ss,ref}$  and  $\theta_{efolding}$  are derived from the analytical expressions  
319 given in Appendix B (Equations 27 and 29). Therefore, both  $r_{ss,ref}$  and  
320  $\theta_{efolding}$  vary with meteorological conditions at the 30-minute time step.
- 321 • For PdS86,  $r_{ss,ref}$  and  $\theta_{efolding}$  are set to the average of the M16 values  
322 during the whole time period. Therefore, both  $r_{ss,ref}$  and  $\theta_{efolding}$  are  
323 constant in this case.

#### 324 4.2. Calibrating $\tau_{hyst}$

325 Figure 5 plots the 30-minute EC-derived SEE as a function of  $\delta t = t - 12$   
326 for two days of period  $P0$ . The linear fit of the daily relationship is superim-  
327 posed for each day separately. The slope (noted  $\delta SEE/\delta t$ ) of the relationship  
328 observed at the daily time scale between  $SEE_t$  and  $\delta t$  is a decreasing function  
329 of the daily mean SEE. The correlation coefficient between daily  $\delta SEE/\delta t$   
330 and daily SEE is  $-0.90$ . Figure 5 also plots the 30-minute TI-derived SEE  
331 as a function of  $\delta t$ . Although the data points are more scattered around the  
332 daily linear fit than for EC case, the daily slope  $\delta SEE/\delta t$  is consistently  
333 decreasing with the daily mean SEE, as for EC case, with a correlation co-  
334 efficient of  $-0.68$ .

335 Based on the daily relationships discussed above, the time parameter  $\tau_{hyst}$   
336 of Equation (9) is calibrated in a three-step procedure:

- 337 • The daily slope  $\delta SEE/\delta t$  is computed for each day of the study period.

- 338 • The daily slope  $\delta SEE/\delta t$  is correlated with the daily mean SEE for  
339 each day of the study period. The daily mean is obtained by averaging  
340 the 30-minute SEE estimates during daytime.
- 341 • The calibrated  $\tau_{hyst}$  is equal to minus the inverse of the slope of the  
342 relationship between  $\delta SEE/\delta t$  and the daily mean SEE (see Equation  
343 7). Note that  $SEE_{12}$  in Equation (7) is replaced by the daily mean  
344 SEE to reduce uncertainties in quasi instantaneous SEE estimates. The  
345 calibrated value of  $\tau_{hyst}$  is 11 and 9 hours for the EC-derived and TI-  
346 derived SEE case, respectively.

347 Note that the above calibration strategy is valid if the observed relation-  
348 ships between  $SEE_t$  and  $\delta t$  and between  $\delta SEE/\delta t$  and the daily mean SEE  
349 are linear as a first approximation. Moreover, we assume herein that the SEE  
350 at noon ( $SEE_{12}$  in Equation 7) is close to the daily mean SEE. In fact, such  
351 a hypothesis relies on the above linearity assumptions. As a linearity assess-  
352 ment of the  $SEE_t(\delta t)$  relationship, the coefficient of determination (ordinary  
353 R-squared) between EC-derived SEE and time of day is estimated as 0.99  
354 and 0.93 for the wet and dry date of Figure 5 respectively. The R-squared is  
355 slightly degraded to 0.93 and 0.73 respectively for the TI case, due to larger  
356 uncertainties in TI-derived SEE estimates.

## 357 5. Results and discussions

358 The proposed  $r_{ss,t}$  model (Equation 5) is applied to the Sidi Rahal'16 data  
359 set and its performance in terms of SEE estimates is compared with that of  
360 two benchmark models: the M16 (Equation 4) and PdS86  $r_{ss}$  models. It

361 is reminded that PdS86 and M16 differ with regard to the values of  $r_{ss,ref}$   
 362 and  $\theta_{efolding}$ , which vary in time in M16 (according to Equation 27 and 29  
 363 respectively) while they are set to a constant value in PdS86. Results are  
 364 presented and discussed below for a calibration undertaken using EC- and  
 365 TI-derived SEE estimates separately.

### 366 5.1. Models calibrated using EC measurements

#### 367 5.1.1. Calibration parameters

368 The calibration algorithm of  $(\theta_{1/2}, \Delta\theta_{1/2}^{-1})$  is run over each period  $P0-8$  us-  
 369 ing EC-derived SEE estimates. Note that diurnal patterns are not accounted  
 370 for in the determination of  $\theta_{1/2}$  and  $\Delta\theta_{1/2}^{-1}$  parameters. The rationale is that  
 371 both parameters are largely independent of  $\tau_{hyst}$ :  $\theta_{1/2}$  and  $\Delta\theta_{1/2}^{-1}$  make SEE  
 372 vary at the daily scale while  $\tau_{hyst}$  makes SEE vary at the hourly scale around  
 373 the daily mean SEE. Retrieved parameters are reported in Table 2 for data  
 374 with a minimum  $LEp$  value of  $400 \text{ Wm}^{-2}$  and  $100 \text{ Wm}^{-2}$  separately. The  
 375 main idea of those empirical thresholds is 1) to remove SEE estimates under  
 376 low ( $< 100 \text{ Wm}^{-2}$ ) evaporative demand conditions and 2) to qualitatively  
 377 distinguish between relatively low and relatively high demand conditions.  
 378 For data with  $LEp > 100 \text{ Wm}^{-2}$ , a pair  $(\theta_{1/2}, \Delta\theta_{1/2}^{-1})$  is obtained for each  
 379 period  $P0 - 8$ . However there are too few data points with  $LEp > 400$   
 380  $\text{Wm}^{-2}$  during the winter months, hence no parameter is retrieved for  $P1 - 4$   
 381 in this case. EC-derived  $\theta_{1/2}$  and  $\Delta\theta_{1/2}^{-1}$  vary in the range  $0.07 - 0.16 \text{ m}^3\text{m}^{-3}$   
 382 and  $4 - 11 \text{ m}^3\text{m}^{-3}$  respectively, with smaller values of  $\theta_{1/2}$  being associated  
 383 with larger values of  $\Delta\theta_{1/2}^{-1}$  and reciprocally. Note that the extreme values  
 384 of  $\theta_{1/2} = 0.07 \text{ m}^3\text{m}^{-3}$  and  $\Delta\theta_{1/2}^{-1} = 11 \text{ m}^3\text{m}^{-3}$  are both obtained during the  
 385 hottest and driest subperiod  $P7$  (see Table 1).

386 Figure 6 compares the retrieved values of  $\theta_{1/2}$  and  $\Delta\theta_{1/2}^{-1}$  in both cases:  
 387  $LEp > 100 \text{ Wm}^{-2}$  versus  $LEp > 400 \text{ Wm}^{-2}$ . The correlation coefficient (and  
 388 root mean square difference) between both data sets (for EC-derived SEE)  
 389 is 0.97 (0.006  $\text{m}^3\text{m}^{-3}$ ) and 1.0 (0.46  $\text{m}^3\text{m}^{-3}$ ) for retrieved  $\theta_{1/2}$  and  $\Delta\theta_{1/2}^{-1}$ ,  
 390 respectively. The calibration results when discarding the data with  $LEp <$   
 391  $400 \text{ Wm}^{-2}$  are very close to those obtained when including all data with  
 392  $LEp > 100 \text{ Wm}^{-2}$ . Therefore, the calibration parameters are found to be  
 393 quite stable with respect to the evaporative demand conditions. Given that  
 394 calibration results using EC-derived SEE estimates are very consistent for  
 395 two different minimum  $LEp$  values, the lower (and less restrictive) threshold  
 396 value  $LEp > 100 \text{ Wm}^{-2}$  is chosen to assess model results in the rest of the  
 397 paper.

398 The definition of 9 study periods and the application of the same calibra-  
 399 tion procedure to data with  $LEp > 100 \text{ Wm}^{-2}$  and data with  $LEp > 400$   
 400  $\text{Wm}^{-2}$  also allow for evaluating the uncertainties in retrieved parameters.  
 401 The relative uncertainty in  $\theta_{1/2}$  (and  $\Delta\theta_{1/2}^{-1}$ ) for a given time series is esti-  
 402 mated as the absolute difference of the values obtained for data with  $LEp >$   
 403  $100 \text{ Wm}^{-2}$  and data with  $LEp > 400 \text{ Wm}^{-2}$  divided by the average. The  
 404 mean relative uncertainty for  $P0$ ,  $P5 - 8$  (see Table 2) is 3% and 7% for  
 405 retrieved  $\theta_{1/2}$  and  $\Delta\theta_{1/2}^{-1}$ , while the temporal variability (relative to the mean  
 406 value for all periods) is estimated as 19% and 40%, respectively. Such results  
 407 further confirm the robustness of the calibration procedure.

#### 408 5.1.2. SEE results

409  $\theta_{1/2}$  and  $\Delta\theta_{1/2}^{-1}$  are set to 0.12  $\text{m}^3\text{m}^{-3}$  and 4.6  $\text{m}^3\text{m}^{-3}$  respectively as es-  
 410 timated previously for  $P0$  data with a minimum  $LEp$  value of  $100 \text{ W m}^{-2}$ ,

411 and  $\tau_{hyst}$  is set to 11 h. Figure 7 plots the SEE simulated by the calibrated  
 412 PdS86, M16 and new  $r_{ss}$  models as a function of EC-derived SEE. The new  
 413 model outperforms M16 and M16 outperforms PdS86 (statistics are provided  
 414 in Table 3). Especially, the correlation coefficient (and RMSD) between sim-  
 415 ulated and observed SEE is improved from 0.80 to 0.85 (from 0.12 to 0.10)  
 416 with the new model. The representation of SEE at the subhourly time scale  
 417 has also an impact on the slope of the linear regression between modeled  
 418 and observed SEE, increasing from 0.86 to 0.91 for M16 and new model re-  
 419 spectively. The new parameterization thus allows for simply representing the  
 420 SEE decrease associated with the receding evaporation front during daytime.

421 Table 3 also lists the error statistics for each subperiod  $Pi$  ( $i = 1, \dots, 8$ ) us-  
 422 ing model parameters retrieved from  $Pi$  data (from  $P0$  data in parenthesis).  
 423 A lower RMSD is generally obtained by the new model using the subperiod  
 424 calibration, except for  $P3$  when the  $P0$  calibration provides a significantly  
 425 improved RMSD (0.18 instead of 0.24). To further explore the case of  $P3$ ,  
 426 we investigate the SEE simulated by M16 and new model separately as a  
 427 function of EC-derived SEE for data with  $LEp > 100 \text{ W m}^{-2}$  during  $P2$ ,  $P3$   
 428 and  $P7$  (Figure 8). Several different behaviors of the  $SEE(\theta)$  relationship  
 429 are observed during  $P3$ , as evidenced by the presence of three groups of data  
 430 points located significantly above, significantly below and around the 1:1 line  
 431 respectively. Given that the calibration method is dedicated to find the best  
 432 slope ( $\Delta\theta_{1/2}^{-1}$ ) at  $\theta_{1/2}$ , one expects to obtain the best slope of the linear regres-  
 433 sion between simulated and observed SEE by calibrating the model over each  
 434 subperiod separately. Table 3 clearly shows that the slope is systematically  
 435 improved in all cases, including the case of  $P3$ . However, a better slope does

436 not necessarily mean an improved RMSD between simulated and observed  
437 SEE.

438 In summary, it is found that 1) both  $\theta_{1/2}$  and  $\Delta\theta_{1/2}^{-1}$  vary between suc-  
439 cessive drying periods, 2) the representation of this temporal variability by  
440 means of a periodic calibration of  $(\theta_{1/2}, \Delta\theta_{1/2}^{-1})$  enhances SEE estimates, and  
441 3) the long-term calibration (during  $P0$ ) of the SEE model still provides re-  
442 liable results that are generally more accurate than those of the PdS86 and  
443 M16 formulations.

#### 444 5.1.3. Evaporation results

445 Since the target is evaporation, rather than SEE, results are also pre-  
446 sented in terms of evaporation estimates in Figure 7. It is reminded that  $LE$   
447 is derived as  $SEE \times LEp$ . Therefore, given that the same energy balance  
448 model is used to simulate both  $LEp$  and  $LE$ , there should be a perfect equiv-  
449 alence between simulated  $LE$  and simulated  $SEE$ . In practice, if simulated  
450  $SEE$  is accurate compared to  $SEE_{EC}$  ( $=LE_{EC}/LEp$ ), then simulated  $LE$   
451 ( $=SEE \times LEp$ ) should be accurate compared to  $LE_{EC}$ . To further assess the  
452 consistency between SEE and evaporation results, Table 4 reports the corre-  
453 lation coefficient, slope of the linear regression and RMSD between simulated  
454 and measured evaporation at Sidi Rahal site for all data with  $LEp > 100$   
455  $Wm^{-2}$ . Statistics are presented for PdS86, M16 and new models separately,  
456 all three models being calibrated with the same input data set (EC data for  
457  $LEp > 100 Wm^{-2}$ ). While the RMSD is relatively low ( $\leq 35 Wm^{-2}$ ) in all  
458 cases, the correlation coefficient (and slope of the linear regression) increases  
459 from 0.81 (0.89) to 0.85 (0.96) for the PdS86 and new model, respectively.  
460 Such improvement is fully consistent with previous results in terms of SEE

461 estimates.

## 462 5.2. Models calibrated using TI measurements

### 463 5.2.1. Calibration parameters

464 Given that EC measurements are available at few locations only, we now  
465 investigate the applicability of the calibration algorithm of  $(\theta_{1/2}, \Delta\theta_{1/2}^{-1})$  to  
466 TI data. In practice, the calibration procedure is applied to TI-derived SEE  
467 estimates over each period  $P0 - 8$ . Retrieved parameters are reported in  
468 Table 5 for data with a minimum  $LEp$  value of  $400 \text{ Wm}^{-2}$  and  $100 \text{ Wm}^{-2}$   
469 separately. TI-derived  $\theta_{1/2}$  and  $\Delta\theta_{1/2}^{-1}$  vary in the range  $0.06 - 0.16 \text{ m}^3\text{m}^{-3}$   
470 and  $4 - 23 \text{ m}^3\text{m}^{-3}$  respectively. Consistent with EC case, smaller values  
471 of TI-derived  $\theta_{1/2}$  are associated with larger values of TI-derived  $\Delta\theta_{1/2}^{-1}$  and  
472 reciprocally. However, in contrast to EC case, the TI-derived  $\Delta\theta_{1/2}^{-1}$  for data  
473 with  $LEp > 100 \text{ Wm}^{-2}$  is about twice the value obtained for data with  
474  $LEp > 400 \text{ Wm}^{-2}$ , while the TI-derived  $\theta_{1/2}$  for data with  $LEp > 100 \text{ Wm}^{-2}$   
475 is about one third lower than the value obtained for data with  $LEp > 400$   
476  $\text{Wm}^{-2}$  (see Figure 6).

477 Figure 9 plots TI-derived versus EC-derived  $\theta_{1/2}$  and  $\Delta\theta_{1/2}^{-1}$  for all periods  
478  $P0 - 8$  and for data with a minimum  $LEp$  value of 100 and  $400 \text{ Wm}^{-2}$   
479 separately. It is clear that a better match of retrieved parameters is obtained  
480 when  $LEp > 400 \text{ Wm}^{-2}$  than when  $LEp > 100 \text{ Wm}^{-2}$ . In fact, the TI-  
481 derived SEE greatly overestimates the EC-derived SEE in conditions of low  
482  $LEp$  values. In relatively wet conditions for instance (see Figure 3), the  
483 TI-derived evaporation (estimated as  $SEE_{TI} \times LEp$ ) can even exceed the  
484 potential evaporation. The above results confirm the applicability domain of  
485 the energy balance model to conditions with  $LEp > 400 \text{ W m}^{-2}$ . Therefore

486 the calibration of the pair  $(\theta_{1/2}, \Delta\theta_{1/2}^{-1})$  using TI-derived SEE data should be  
487 carried out under relatively large  $LEp$  conditions only.

488 The systematic difference between EC- and TI-derived SEE under low  
489  $LEp$  conditions can be explained by the inconsistency between the soil tem-  
490 perature modeled at the evaporation front (Equation 1) and the remotely  
491 sensed radiometric temperature that is representative of the surface skin  
492 temperature only. In fact, the soil temperature modeled in dry conditions  
493  $T_{dry}$  is expected to deviate from the top soil temperature in the presence of  
494 a receding evaporation front (Or et al., 2013). There are methods to correct  
495 this inconsistency. For instance two distinct approaches have been devel-  
496 oped to relate the observed superficial temperature to deeper soil tempera-  
497 tures, either by implementing a physically-based heat diffusion model (Bateni  
498 et al., 2013) to dynamically constrain the modeled surface temperature from  
499 deeper temperatures or by smoothing/lagging the surface temperature using  
500 a Fourier dissipation (Heusinkveld et al., 2004; Gentine et al., 2011) or lag  
501 (Gentine et al., 2012) model.

502 The relative uncertainty in the  $(\theta_{1/2}$  and  $\Delta\theta_{1/2}^{-1})$  parameters retrieved from  
503 TI data is estimated by computing the absolute difference of the values ob-  
504 tained for TI data with  $LEp > 400 \text{ Wm}^{-2}$  and for EC data with  $LEp > 100$   
505  $\text{Wm}^{-2}$  divided by the average. The mean relative uncertainty for  $P0$ ,  $P5 - 8$   
506 (see Tables 2 and 5) is 8% and 21% for retrieved  $\theta_{1/2}$  and  $\Delta\theta_{1/2}^{-1}$ , respectively.  
507 Although EC-retrieved parameters (3% and 7% relative error, respectively)  
508 are more accurate than TI-derived parameters, the temporal variability in  
509 retrieved parameters (19% and 40%, respectively) remains larger, i.e. cali-  
510 bration using TI data is still effective and meaningful. Such results further

511 confirm the consistency between TI- and EC-derived SEE estimates when  
512  $LEp > 400 \text{ Wm}^{-2}$ .

### 513 5.2.2. SEE results

514 The hysteretic parameter  $\tau_{hyst}$  is set to 9 h and the pair  $(\theta_{1/2}, \Delta\theta_{1/2}^{-1})$  is  
515 set to (0.085, 10.0) and (0.125, 4.21) as estimated with the P0 TI data for a  
516 minimum  $LEp$  value of 100 and 400  $\text{W m}^{-2}$ , respectively. Table 6 reports  
517 error statistics in terms of correlation coefficient, slope of the linear regression  
518 and RMSD between simulated and EC-derived SEE for all  $LEp$  conditions  
519 ( $LEp > 100 \text{ W m}^{-2}$ ). Best results are highlighted in bold. Consistent  
520 with EC case, the correlation coefficient between simulated and observed  
521 SEE is improved from 0.77 to 0.81 and from 0.80 to 0.86 when including  
522 time of day in the soil resistance for data with  $LEp > 100$  and  $LEp > 400$   
523  $\text{Wm}^{-2}$ , respectively. Moreover, the error statistics for data with  $LEp > 400$   
524  $\text{Wm}^{-2}$  are very similar to those obtained with the EC, with a correlation  
525 coefficient of 0.86 and a RMSD of 0.10. Only the slope of the linear regression  
526 between simulated and observed SEE is degraded from 0.91 (EC case) to  
527 0.87 (TI case). Results in terms of SEE estimates are logically superior when  
528 calibrating the model using TI data with  $LEp > 400 \text{ Wm}^{-2}$  than using TI  
529 data with  $LEp > 100 \text{ Wm}^{-2}$ , as the actual to wet temperature difference is  
530 a good indicator of water stress when energy is not limiting (Boulet et al.,  
531 2007).

532 Table 6 also lists the error statistics for each subperiod  $Pi$  ( $i = 1, \dots, 8$ )  
533 using model parameters retrieved from the data set corresponding to sub-  
534 period  $Pi$  and  $LEp > 100 \text{ Wm}^{-2}$  and from the data set corresponding to  
535 P0 and  $LEp > 400 \text{ Wm}^{-2}$  (in parenthesis). The new SEE formulation gen-

536 erally provides best results in terms of correlation coefficient, slope of the  
 537 linear regression and RMSD between simulated and observed SEE. However,  
 538 the calibration of  $(\theta_{1/2}, \Delta\theta_{1/2}^{-1})$  by subperiod does not succeed in representing  
 539 the temporal variability of model parameters, which is due to the system-  
 540 atic bias in TI-derived SEE for low  $LEp$  values. The relatively large slope  
 541 (1.25 for  $P0$ ) of the linear regression between simulated and observed SEE  
 542 for data with  $LEp > 100 \text{ Wm}^{-2}$  also reflects the overestimation of SEE by  
 543 using TI data under low evaporative demand conditions. On the contrary,  
 544 the calibration of  $(\theta_{1/2}, \Delta\theta_{1/2}^{-1})$  over the whole period  $P0$  using TI data with  
 545  $LEp > 400 \text{ Wm}^{-2}$  provides good results at the subperiod scale (during each  
 546 period  $P1 - 8$ ).

547 In summary, the above results indicate that 1) the calibration of model  
 548 parameters is feasible using TI data and 2) selecting TI data collected under  
 549 relatively high evaporative demand conditions ( $LEp > 400 \text{ Wm}^{-2}$  herein) is  
 550 required for obtaining similar accuracy to the EC-based calibration case.

### 551 *5.3. Applicability to temporally-sparse thermal data*

552 The new  $r_{ss}$  formulation of Equation (5) is based on three parameters:  
 553  $\tau_{hyst}$ ,  $\theta_{1/2}$  and  $\Delta\theta_{1/2}^{-1}$ . Validation results at Sidi Rahal site have shown that  
 554 all three parameters can be efficiently calibrated using TI data combined  
 555 with meteorological forcing and near-surface soil moisture observations. This  
 556 opens up the path for model calibration using spaceborne thermal-derived  
 557 radiometric surface temperature. However, the spatio-temporal resolution  
 558 of available remote sensing products may be in some cases inadequate for  
 559 implementing such a calibration. In particular, the thermal data available at  
 560 high (100 m) spatial resolution have a repeat cycle of 8 days (by combining

561 Landsat-7 and Landsat-8) only or more, depending on cloudy/non-cloudy  
562 conditions on Landsat overpass dates.

563 This subsection aims to assess the applicability of the calibration ap-  
564 proach of  $(\theta_{1/2}, \Delta\theta_{1/2}^{-1})$  to temporally sparse thermal data. In practice, pa-  
565 rameter  $\tau_{hyst}$  is set to 9 hours (as retrieved from high frequency TI data) and  
566 the observation cycle of available TI data is increased from the hourly time  
567 scale (previous results) to the 1-day, 2-day, 3-day, 4-day, 5-day, 6-day, 7-day  
568 and the 8-day period (Landsat repeat cycle), and model results are evalu-  
569 ated in each case. Note that the 1-day repeat cycle mimics the availability of  
570 MODIS (MODerate resolution Imaging Spectroradiometer) TI data collected  
571 onboard Terra and Aqua at 1 km resolution. To quantitatively evaluate the  
572 uncertainty in retrieved parameters and model outputs (SEE and LE), an  
573 input ensemble is built at a given TI observation cycle by extracting the TI  
574 data at 11:30am, 12:00pm and 12:30pm separately and, for observation cycles  
575 larger than 1 day, by including all the possible independent time series shifted  
576 by 1 day from one another. The acquisition time approximately corresponds  
577 to the overpass time (from 10:30am to 1:30pm) of available thermal sensors  
578 at 100 m and 1 km resolution. For the hourly observation cycle, the ensemble  
579 of input parameter sets is composed of the 3  $(\theta_{1/2}, \Delta\theta_{1/2}^{-1})$  pairs retrieved dur-  
580 ing the whole study period using EC data with  $LEp > 100 \text{ Wm}^{-2}$ , EC data  
581 with  $LEp > 400 \text{ Wm}^{-2}$  and TI data with  $LEp > 400 \text{ Wm}^{-2}$ . For the other  
582 cases (observation cycles equal to 1 day or more), TI data with  $LEp > 400$   
583  $\text{Wm}^{-2}$  are used.

584 Figure 10 presents model results as a function of an increasing TI ob-  
585 servation cycle. The calibration results in terms of retrieved  $\theta_{1/2}$  and  $\Delta\theta_{1/2}^{-1}$

586 correspond to data with  $LEp > 400 \text{ Wm}^{-2}$  while the model output results  
 587 in terms of SEE and LE correspond to all data with  $LEp > 100 \text{ Wm}^{-2}$ .  
 588 The mean retrieved  $\theta_{1/2}$  is found to be remarkably stable for all observation  
 589 cycles ranging from 0 to 8 days, although its standard deviation significantly  
 590 increases for an observation cycle changing from 1 to 2 days. The mean re-  
 591 trieved  $\Delta\theta_{1/2}^{-1}$  is systematically biased by about +20% for an observation cycle  
 592 ranging from 1 to 8 days, and the variability of the retrieved  $\Delta\theta_{1/2}$  within  
 593 each input ensemble is relatively large (20–50%) for observation cycles 2-8  
 594 days. The relatively large variability of  $\Delta\theta_{1/2}^{-1}$  is attributed to the lack of ther-  
 595 mal observations with both wet soil and  $LEp > 400 \text{ Wm}^{-2}$  conditions. Note  
 596 that such a limitation is specific to rainfed semi-arid areas like the Sidi Rahal  
 597 region. Finally, as an assessment of the calibration strategy,  $LE$  estimates  
 598 are compared for three different calibration approaches of  $r_{ss,ref}$  and  $\theta_{efolding}$ :  
 599 the fixed parameters (S92) of Sellers et al. (1992), the pedotransfer function  
 600 (M16) in Merlin et al. (2016) and the proposed TI-based calibration. The  
 601 mean root mean square error (RMSE) between simulated and EC-derived  
 602  $LE$  is about 60, 50 and 40  $\text{Wm}^{-2}$  for the S92, M16 and TI-based calibra-  
 603 tion strategy, respectively. Such results emphasize the utility of calibrating  
 604 evaporation models using thermal data, even when TI data are temporally  
 605 sparse.

## 606 **6. Conclusions and perspectives**

607 A new  $r_{ss}$  formulation is proposed to improve soil evaporative efficiency  
 608 (SEE) estimates at the subhourly time scale given the near-surface (0 – 5  
 609 cm) soil moisture, time of day and meteorological forcing data. The model

610 builds on the recent M16 SEE model and integrates time of day to implicitly  
 611 represent the impact of the receding evaporation front on quasi instantaneous  
 612 SEE during daytime. The three model parameters namely  $\theta_{1/2}$ ,  $\Delta\theta_{1/2}^{-1}$  and  
 613  $\tau_{hyst}$  are calibrated using Eddy-covariance (EC) measurements collected at a  
 614 bare soil field (Sidi Rahal site) in central Morocco. Results in terms of corre-  
 615 lation coefficient, slope of the linear regression and RMSD between simulated  
 616 and observed SEE indicate that the new model clearly outperforms both M16  
 617 and also PdS86, which is classically used in many land surface models. Given  
 618 that EC measurements are available at few locations only, the applicability  
 619 of the calibration approach is also tested using thermal infrared (TI) instead  
 620 of EC data. It is found that TI-derived SEE overestimates EC-derived SEE  
 621 under low  $LEp$  ( $< 400 \text{ Wm}^{-2}$ ) conditions. However, the model calibration  
 622 using TI data under relatively high  $LEp$  ( $> 400 \text{ Wm}^{-2}$ ) conditions provides  
 623 very similar SEE results to the EC-based calibration case.

624 The phenomenological modeling approach allows to represent instanta-  
 625 neous SEE over long time periods using a limited number (3) of input pa-  
 626 rameters. Moreover, the hysteretic parameter  $\tau_{hyst}$  (controlling the intrusion  
 627 of evaporation front during daytime under given  $LEp$  and  $\theta$  conditions) re-  
 628 trieved at the Sidi Rahal site is found to be fairly stable during the 9-month  
 629 study period. Both  $\theta_{1/2}$  and  $\Delta\theta_{1/2}^{-1}$  parameters (controlling the nonlinear SEE  
 630 response to  $\theta$ ) vary between two successive drying periods, but accurate SEE  
 631 estimates are still obtained when considering those paramaters as constant  
 632 during the whole study period. An alternative calibration scheme could be  
 633 the calibration of a single parameter ( $\tau_{hyst}$ ), while the others ( $\theta_{1/2}, \Delta\theta_{1/2}^{-1}$ )  
 634 being estimated using pedotransfer functions as proposed in (Merlin et al.,

635 2016). Nonetheless, two questions that still remain open are the spatial vari-  
636 ability of  $\tau_{hyst}$  and the temporal variability of  $(\theta_{1/2}, \Delta\theta_{1/2}^{-1})$ . **Additional vali-**  
637 **dation under different conditions is needed as a single site under the semi-arid**  
638 **climate of Morocco is used in this study to develop and evaluate the method.**  
639 Also, it is difficult to provide a deep, and quantitative, physical understand-  
640 ing of the origin of this variability using a downward/semi-empirical modeling  
641 framework solely. Future studies based on a mechanistic model could address  
642 the issue of interpreting temporally-variable parameters. Moreover, the en-  
643 ergy balance model used in this study to relate SEE to evaporation has been  
644 successfully evaluated in terms of  $T_{wet}$  and  $T_{dry}$  in Stefan et al. (2015) but  
645 not in terms of  $LEp$  directly. Although simulated  $LEp$  values are very con-  
646 sistent with EC  $LE$  observations ( $SEE_{EC} = LE_{EC}/LEp$  consistently ranges  
647 between 0 and 1), further research should be undertaken to quantitatively  
648 evaluate  $LEp$  estimates. This would require a specific experiment where soil  
649 is maintained at field capacity under various atmospheric forcing conditions  
650 (during several weeks).

651 The coupling of the new  $r_{ss}/SEE$  formulation with microwave-derived  
652 soil moisture and thermal-derived radiometric temperature would allow soil  
653 evaporation to be estimated at multiple scales over large areas. **However, the**  
654 **concurrent requirements -to calibrate the model's parameters- of high evap-**  
655 **orative demand (a threshold of  $400 \text{ W m}^{-2}$  is used in this study), rainfall**  
656 **or irrigation events (enough to produce soil moisture variability) but lack of**  
657 **clouds, so that thermal satellite images can be acquired, and bare soil sur-**  
658 **faces for relatively long periods are difficult to reach with current satellites.**  
659 **In fact, the model calibration over areas of agricultural or ecological interest**

660 requires remote sensing data at high spatio-temporal resolution (Lagouarde  
661 et al., 2013, e.g.). As a long-term vision, the integration of the  $r_{ss}$  parameter-  
662 ization in state-of-the-art dual-source surface models (Norman et al., 1995,  
663 e.g.) has great potential to help separate soil evaporation and plant transpi-  
664 ration components of agricultural crops (Merlin et al., 2014, e.g.), and hence  
665 to better assess the crop water use efficiency. Under vegetated surface, soil  
666 evaporation would be affected not only by the soil available energy but also  
667 by the heat and vapor transfer coefficients between the soil, vegetation and  
668 atmosphere (Shuttleworth and Wallace, 1985; Haghghi and Or, 2015). In  
669 the recent study of Hssaine et al. (2018), the soil resistance’s parameters were  
670 calibrated over partially covering wheat by implementing a network of soil,  
671 vegetation and air resistances and by separating phenological stages with  
672 fractional vegetation cover smaller and larger than 0.5. Further research  
673 should tackle the structural (radiation interception) and functional (tran-  
674 spiration rate) vegetation effects of different biomes on the soil evaporation  
675 underneath. Last but not least, future studies should investigate the impact  
676 on evaporation estimates (and calibration parameters) of uncertainties in in-  
677 put soil moisture data sets derived from active microwave, passive microwave,  
678 disaggregation and/or assimilation techniques (Peng et al., 2017).

#### 679 **A. Soil energy balance model**

680 The evaporation model classically solves the energy budget equation over  
681 bare soil:

$$LE = Rn - G - H \quad (13)$$

682 with  $LE$  ( $\text{W m}^{-2}$ ) being the soil latent heat flux,  $H$  ( $\text{W m}^{-2}$ ) the soil sensible  
683 heat flux,  $Rn$  ( $\text{W m}^{-2}$ ) the soil net radiation and  $G$  ( $\text{W m}^{-2}$ ) the ground  
684 conduction at 5-cm depth. The soil net radiation is expressed as:

$$Rn = (1 - \alpha)R_g + \epsilon(R_a - \sigma T^4) \quad (14)$$

685 with  $\alpha$  (-) being the soil albedo,  $R_g$  ( $\text{W m}^{-2}$ ) the incoming solar radiation,  
686  $\epsilon$  (-) the soil emissivity (set to 0.95),  $R_a$  ( $\text{W m}^{-2}$ ) the atmospheric longwave  
687 radiation,  $\sigma$  ( $\text{Wm}^{-2}\text{K}^{-4}$ ) the Stefan-Boltzmann constant and  $T$  (K) the soil  
688 skin temperature. For simplicity,  $\alpha$  is set to a constant value (0.20) as in  
689 (Merlin et al., 2016). When applied to low resolution remote sensing data,  
690 albedo could be made variable as a function of surface soil composition and  
691 moisture (Liu et al., 2014). The downward atmospheric radiation at ground  
692 level is expressed as:

$$R_a = \epsilon_a \sigma T_a^4 \quad (15)$$

693 with  $\epsilon_a$  (-) being the effective atmospheric emissivity, and  $T_a$  (K) the air  
694 temperature. The emissivity of clear skies is estimated as in Brutsaert (1975):

$$\epsilon_a = 0.553(e_a/100)^{1/7} \quad (16)$$

695 with:

$$e_a = e_{sat}(T_a)(h_a/100) \quad (17)$$

696 with  $h_a$  (%) being the air relative humidity and:

$$e_{sat}(T_a) = 611 \exp \left[ 17.27 (T_a - 273.2)/(T_a - 35.9) \right] \quad (18)$$

697 with  $T_a$  in K. The ground conduction is estimated as a fraction of soil net  
698 radiation (Choudhury et al., 1987; Kustas and Daughtry, 1990):

$$G = C_G Rn \quad (19)$$

699 with  $C_G$  (-) a coefficient (set to 0.20). The sensible heat flux is expressed as:

$$H = \rho C_P \frac{T - T_a}{r_{ah}} \quad (20)$$

700 with the aerodynamic resistance being estimated as in Choudhury et al.  
701 (1986):

$$r_{ah} = \frac{r_{ah0}}{(1 + Ri)^\eta} \quad (21)$$

702 with  $r_{ah0}$  ( $\text{s m}^{-1}$ ) being the neutral aerodynamic resistance and  $Ri$  (-) the  
703 Richardson number, which represents the importance of free versus forced  
704 convection, and  $\eta$  (-) a coefficient set to 0.75 in unstable conditions ( $T > T_a$ )  
705 and to 2 in stable conditions ( $T < T_a$ ). The neutral  $r_{ah0}$  is computed as:

$$r_{ah0} = \frac{1}{k^2 u_a} \left[ \ln \left( \frac{Z}{z_{0m}} \right) \right]^2 \quad (22)$$

706 with  $k$  (-) being the von Karman constant,  $u_a$  ( $\text{m s}^{-1}$ ) the wind speed mea-  
707 sured at the reference height  $Z$  (m) and  $z_{0m}$  (m) the momentum soil rough-  
708 ness (set to 0.001 m (Yang et al., 2008; Stefan et al., 2015; Merlin et al.,  
709 2016)). The Richardson number is computed as:

$$Ri = \frac{5gZ(T - T_a)}{T_a u_a^2} \quad (23)$$

710 with  $g$  ( $\text{m s}^{-2}$ ) being the gravitational constant. The energy balance of  
711 Equation (13) is solved by initializing the surface soil temperature  $T = T_a$ ,  
712 and by looking for the value of  $T$  that minimizes the cost function  $F(T)$ :

$$F(T) = (LE + H - Rn + G)^2 \quad (24)$$

713 with  $LE$  being expressed as in Equation 1.

714 **B. Analytical expressions of  $r_{ss,ref}$  and  $\theta_{efolding}$**

715 As an attempt to approximate SEE over its full range  $[0 - 1]$ , SEE is  
 716 approached linearly at the mid-value (0.5). The linear approximation of  
 717  $SEE(\theta)$  at  $SEE = 0.5$  sets two constraints on the model. First, the soil  
 718 moisture value at which  $SEE = 0.5$  is noted  $\theta_{1/2}$ :

$$SEE(\theta_{1/2}) = 0.5 \quad (25)$$

719 Second, the first derivative of SEE at  $\theta_{1/2}$  is set to the slope ( $\Delta\theta_{1/2}^{-1}$ ) of the  
 720 linear regression between SEE and  $\theta$  observations:

$$\left(\frac{\partial SEE}{\partial \theta}\right)(\theta_{1/2}) = \Delta\theta_{1/2}^{-1} \quad (26)$$

721 The combination of the above two equations allows to estimate both  $r_{ss,ref}$   
 722 and  $\theta_{efolding}$  parameters given a time series of SEE and  $\theta$  observations. Pa-  
 723 rameters  $r_{ss,ref}$  and  $\theta_{efolding}$  in Equation (4) are analytically expressed as a  
 724 function of  $\theta_{1/2}$ ,  $\Delta\theta_{1/2}^{-1}$ , soil temperature ( $T_{wet}$  and  $T_{1/2}$ ) and aerodynamic  
 725 resistance ( $r_{ah,wet}$  and  $r_{ah,1/2}$ ) values corresponding to  $r_{ss} = 0$  and  $\theta = \theta_{1/2}$ ,  
 726 respectively. The soil energy balance model described in Appendix A is used  
 727 to estimate both pairs ( $T_{wet}, r_{ah,wet}$ ) and ( $T_{1/2}, r_{ah,1/2}$ ) for a given meteorolo-  
 728 gical forcing.

729 Briefly,  $r_{ss,ref}$  is derived by inverting Equation (4):

$$r_{ss,ref} = r_{ss,1/2} \exp(\theta_{1/2}/\theta_{efolding}) \quad (27)$$

730 with  $r_{ss,1/2}$  being the soil resistance at  $\theta_{1/2}$  obtained by combining Equations  
 731 (3) and (25):

$$r_{ss,1/2} = 2 \frac{e_{sat}(T_{1/2}) - e_a}{e_{sat}(T_{wet}) - e_a} r_{ah,wet} - r_{ah,1/2} \quad (28)$$

732  $\theta_{efolding}$  is obtained by applying the first derivative at  $\theta = \theta_{1/2}$  to the soil  
 733 energy balance equation:

$$\theta_{efolding} = \frac{\frac{r_{ss,1/2}}{r_{ss,1/2}+r_{ah,1/2}}(e_{sat}(T_{1/2}) - e_a) + f(\theta_{1/2})\dot{e}_{sat}(T_{1/2})}{\frac{r_{ss,1/2}+r_{ah,1/2}}{r_{ah,wet}}(e_{sat}(T_{wet}) - e_a)} \times \frac{1}{\Delta\theta_{1/2}^{-1}} \quad (29)$$

734 with  $\dot{e}_{sat}$  being the derivative of saturated vapor pressure with respect to  $T$   
 735 and  $f(\theta_{1/2})$  expressed as:

$$f(\theta_{1/2}) = -\frac{\frac{r_{ss,1/2}r_{ah,1/2}}{(r_{ss,1/2}+r_{ah,1/2})^2}(e_{sat}(T_{1/2}) - e_a)}{\gamma + \frac{r_{ah,1/2}}{r_{ss,1/2}+r_{ah,1/2}}\dot{e}_{sat}(T_{1/2}) + 4\frac{\gamma}{\rho C_P}\epsilon\sigma(1 - C_G)T_{1/2}^3 r_{ah,1/2}} \quad (30)$$

736 Note that the full analytical development of  $\theta_{efolding}$  is described in Merlin  
 737 et al. (2016).

## 738 Acknowledgments

739 This study was supported by the French Agence Nationale de la Recherche  
 740 (MIXMOD-E project, ANR-13-JS06-003-01) and the European Commission  
 741 Horizon 2020 Programme for Research and Innovation (H2020) in the con-  
 742 text of the Marie Skłodowska-Curie Research and Innovation Staff Exchange  
 743 (RISE) action (REC project, grant agreement no: 645642). Initial set up and  
 744 maintenance of the Sidi Rahal station are funded by the Joint International  
 745 Laboratory TREMA <http://trema.ucam.ac.ma>.

746 **References**

- 747 Agam, N., Evett, S. R., Tolk, J. A., Kustas, W. P., Colaizzi, P. D., Alfieri,  
748 J. G., McKee, L. G., Copeland, K. S., Howell, T. A., Chávez, J. L., 2012.  
749 Evaporative loss from irrigated interrows in a highly advective semi-arid  
750 agricultural area. *Adv. Water Resour.* 50, 20–30.
- 751 Allen, S., 1990. Measurement and estimation of evaporation from soil under  
752 sparse barley crops in northern syria. *Agr. For. Meteorol.* 49 (4), 291–309.
- 753 Bateni, S., Entekhabi, D., Castelli, F., 2013. Mapping evaporation and esti-  
754 mation of surface control of evaporation using remotely sensed land surface  
755 temperature from a constellation of satellites. *Water Resour. Res.* 49 (2),  
756 950–968.
- 757 Boone, A., Samuelsson, P., Gollvik, S., Napoly, A., Jarlan, L., Brun, E.,  
758 Decharme, B., 2017. The interactions between soil-biosphere-atmosphere  
759 land surface model with a multi-energy balance (isba-meb) option in  
760 surfexv8-part 1: Model description. *Geosci. Model Dev.* 10 (2), 843.
- 761 Boulet, G., Chehbouni, A., Gentine, P., Duchemin, B., Ezzahar, J., Hadria,  
762 R., 2007. Monitoring water stress using time series of observed to un-  
763 stressed surface temperature difference. *Agr. For. Meteorol.* 146, 157–172.
- 764 Brutsaert, W., 1975. On a derivable formula for long-wave radiation from  
765 clear skies. *Water Resour. Res.* 11 (5), 742–744.
- 766 Caparrini, F., Castelli, F., Entekhabi, D., 2004. Variational estimation of soil  
767 and vegetation turbulent transfer and heat flux parameters from sequences  
768 of multisensor imagery. *Water Resour. Res.* 40 (12).

- 769 Chanzy, A., Bruckler, L., 1993. Significance of soil surface moisture with  
770 respect to daily bare soil evaporation. *Water Resour. Res.* 29 (4), 1113–  
771 1125.
- 772 Chanzy, A., Bruckler, L., Perrier, A., 1995. Soil evaporation monitoring: a  
773 possible synergism of microwave and infrared remote sensing. *J. Hydrol.*  
774 165, 235–259.
- 775 Choudhury, B., Idso, S. B., Reginato, R. J., 1987. Analysis of an empirical  
776 model for soil heat flux under a growing wheat crop for estimating evap-  
777 oration by an infrared-temperature based energy balance equation. *Agr.*  
778 *For. Meteorol.* 39 (4), 283–297.
- 779 Choudhury, B., Reginato, R. J., Idso, S. B., 1986. An analysis of infrared  
780 temperature observations over wheat and calculation of latent heat flux.  
781 *Agr. For. Meteorol.* 37, 75–88.
- 782 Coenders-Gerrits, A., Van der Ent, R., Bogaard, T., Wang-Erlandsson, L.,  
783 Hrachowitz, M., Savenije, H., 2014. Uncertainties in transpiration esti-  
784 mates. *Nature* 506 (7487), E1–E2.
- 785 Decker, M., Or, D., Pitman, A., Ukkola, A., 2017. New turbulent resistance  
786 parameterization for soil evaporation based on a pore scale model: Impact  
787 on surface fluxes in cable. *J. Adv. Model. Earth Sys.*
- 788 Dickinson, R. E., Henderson-Sellers, A., Kennedy, P. J., Wilson, M. F., 1986.  
789 Biosphere-Atmosphere Transfer Scheme (BATS) for the NCAR Commu-  
790 nity Climate model. National Center for Atmospheric Research Technical  
791 Note, Boulder, Colorado.

- 792 Ershadi, A., McCabe, M., Evans, J. P., Chaney, N. W., Wood, E. F., 2014.  
793 Multi-site evaluation of terrestrial evaporation models using fluxnet data.  
794 Agr. For. Meteorol. 187, 46–61.
- 795 Gentine, P., Entekhabi, D., Heusinkveld, B., 2012. Systematic errors in  
796 ground heat flux estimation and their correction. Water Resour. Res.  
797 48 (9).
- 798 Gentine, P., Polcher, J., Entekhabi, D., 2011. Harmonic propagation of  
799 variability in surface energy balance within a coupled soil-vegetation-  
800 atmosphere system. Water Resour. Res. 47 (5).
- 801 Gutmann, E. D., Small, E. E., 2007. A comparison of land surface model  
802 soil hydraulic properties estimated by inverse modeling and pedotransfer  
803 functions. Water Resour. Res. 43, W05418.
- 804 Haghghi, E., Or, D., 2015. Linking evaporative fluxes from bare soil across  
805 surface viscous sublayer with the Monin–Obukhov atmospheric flux-profile  
806 estimates. Journal of Hydrology 525, 684–693.
- 807 Haghghi, E., Shahrane, E., Lehmann, P., Or, D., 2013. Evaporation rates  
808 across a convective air boundary layer are dominated by diffusion. Water  
809 Resour. Res. 49 (3), 1602–1610.
- 810 Hain, C. R., Mecikalski, J. R., Anderson, M. C., 2009. Retrieval of an avail-  
811 able water-based soil moisture proxy from thermal infrared remote sensing.  
812 part i: Methodology and validation. J. Hydrometeorol. 10 (3), 665–683.

- 813 Heitman, J. L., Xiao, X., Horton, R., Sauer, T. J., 2008. Sensible heat mea-  
814 surements indicating depth and magnitude of subsurface soil water evap-  
815 oration. *Water Resour. Res.* 44, W00D05.
- 816 Heusinkveld, B., Jacobs, A., Holtslag, A., Berkowicz, S., 2004. Surface energy  
817 balance closure in an arid region: role of soil heat flux. *Agr. For. Meteorol.*  
818 122 (1), 21–37.
- 819 Hssaine, B. A., Merlin, O., Rafi, Z., Ezzahar, J., Jarlan, L., Khabba, S.,  
820 Er-Raki, S., 2018. Calibrating an evapotranspiration model using radio-  
821 metric surface temperature, vegetation cover fraction and near-surface soil  
822 moisture data. *Agr. For. Meteorol.* 256, 104–115.
- 823 Jarlan, L., Khabba, S., Er-Raki, S., Le Page, M., Hanich, L., Fakir, Y.,  
824 Merlin, O., Mangiarotti, S., Gascoin, S., Ezzahar, J., et al., 2015. Remote  
825 sensing of water resources in semi-arid mediterranean areas: The joint  
826 international laboratory trema. *Int. J. Remote Sens.* 36 (19-20), 4879–  
827 4917.
- 828 Khabba, S., Jarlan, L., Er-Raki, S., Le Page, M., Ezzahar, J., Boulet, G.,  
829 Simonneaux, V., Kharrou, M., Hanich, L., Chehbouni, G., 2013. The  
830 SudMed program and the Joint International Laboratory TREMA: A  
831 decade of water transfer study in the Soil-Plant-Atmosphere system over  
832 irrigated crops in semi-arid area. *Procedia Environ. Sci.* 19, 524–533.
- 833 Kool, D., Agam, N., Lazarovitch, N., Heitman, J. L., Sauer, T. J., Ben-Gal,  
834 A., 2014. A review of approaches for evapotranspiration partitioning. *Agr.*  
835 *For. Meteorol.* 184, 56–70.

- 836 Kustas, W. P., Daughtry, C. S. T., 1990. Estimation of the soil heat flux/net  
837 radiation ratio from spectral data. *Agr. For. Meteorol.* 49, 205–223.
- 838 Kustas, W. P., Norman, J. M., 1999. Evaluation of soil and vegetation heat  
839 flux predictions using a simple two-source model with radiometric temper-  
840 atures for partial canopy cover. *Agr. For. Meteorol.* 94 (1), 13–29.
- 841 Lagouarde, J.-P., Bach, M., Sobrino, J. A., Boulet, G., Briottet, X., Cher-  
842 chali, S., Coudert, B., Dadou, I., Dedieu, G., Gamet, P., et al., 2013. The  
843 mistigri thermal infrared project: scientific objectives and mission specifi-  
844 cations. *Int. J. Remote Sens.* 34 (9-10), 3437–3466.
- 845 Lhomme, J.-P., Chehbouni, A., 1999. Comments on dual-source vegetation-  
846 atmosphere transfer models. *Agr. For. Meteorol.* 94 (3), 269–273.
- 847 Li, F., Kustas, W. P., Anderson, M. C., Jackson, T. J., Bindlish, R., Prueger,  
848 J. H., 2006. Comparing the utility of microwave and thermal remote-  
849 sensing constraints in two-source energy balance modeling over an agri-  
850 cultural landscape. *Remote Sens. Environ.* 101 (3), 315–328.
- 851 Liu, S., Roujean, J.-L., Tchuente, A. T. K., Ceamanos, X., Calvet, J.-C.,  
852 2014. A parameterization of seviri and modis daily surface albedo with  
853 soil moisture: Calibration and validation over southwestern france. *Remote*  
854 *Sens. Environ.* 144, 137–151.
- 855 Mahrt, L., Pan, H., 1984. A two-layer model of soil hydrology. *Bound. Layer*  
856 *Meteorol.* 29, 1–20.
- 857 Merlin, O., 2013. An original interpretation of the wet edge of the surface  
858 temperature-albedo space to estimate crop evapotranspiration (SEB-1S),

- 859 and its validation over an irrigated area in northwestern Mexico. *Hydrol.*  
860 *Earth Syst. Sci.* 17, 3623–3637.
- 861 Merlin, O., Al Bitar, A., Rivalland, V., Béziat, P., Ceschia, E., Dedieu, G.,  
862 2011. An analytical model of evaporation efficiency for unsaturated soil  
863 surfaces with an arbitrary thickness. *J. Appl. Meteor. Clim.* 50 (2), 457–  
864 471, doi:10.1175/2010JAMC2418.1.
- 865 Merlin, O., Chirouze, J., Oliosio, A., Jarlan, L., Chehbouni, G., Boulet, G.,  
866 2014. An image-based four-source surface energy balance model to esti-  
867 mate crop evapotranspiration from solar reflectance/thermal emission data  
868 (SEB-4S). *Agr. For. Meteorol.* 184, 188–203.
- 869 Merlin, O., Stefan, V. G., Amazirh, A., Chanzy, A., Ceschia, E., Er-Raki, S.,  
870 Gentine, P., Tallec, T., Ezzahar, J., Bircher, S., Beringer, J., Khabba, S.,  
871 2016. Modeling soil evaporation efficiency in a range of soil and atmospheric  
872 conditions using a meta-analysis approach. *Water Resour. Res.* 52 (5),  
873 3663–3684.  
874 URL <http://dx.doi.org/10.1002/2015WR018233>
- 875 Molden, D., Oweis, T., Steduto, P., Bindraban, P., Hanjra, M. A., Kijne, J.,  
876 2010. Improving agricultural water productivity: between optimism and  
877 caution. *Agr. Water Manage.* 97 (4), 528–535.
- 878 Norman, J. M., Kustas, W. P., Humes, K. S., 1995. Source approach for  
879 estimating soil and vegetation energy fluxes in observations of directional  
880 radiometric surface temperature. *Agr. For. Meteorol.* 77, 263–293.

- 881 Oleson, K. W., Lawrence, D. M., Bonan, G. B., Drewniak, B., Huang, M.,  
882 Koven, C. D., Levis, S., Li, F., Riley, W. J., Subin, Z. M., Swenson,  
883 S. C., Thornton, P. E., Bozbiyik, A., Fisher, R., Heald, C. L., Kluzek, E.,  
884 Lamarque, J.-F., Lawrence, P. J., Leung, L. R., Lipscomb, W., Muszala, S.,  
885 Ricciuto, D. M., Sacks, W., Sun, Y., Tang, J., Yang, Z.-L., 2013. Technical  
886 Description of version 4.5 of the Community Land Model (CLM). Vol. TN-  
887 503+STR. National Center for Atmospheric Research, Boulder, Colorado.
- 888 Or, D., Lehmann, P., Shahraeeni, E., Shokri, N., 2013. Advances  
889 in Soil Evaporation Physics - A Review. *Vadose Zone J.* 12 (4),  
890 doi:10.2136/vzj2012.0163.
- 891 Paloscia, S., Pettinato, S., Santi, E., Notarnicola, C., Pasolli, L., Reppucci,  
892 A., 2013. Soil moisture mapping using sentinel-1 images: Algorithm and  
893 preliminary validation. *Remote Sens. of Environ.* 134, 234–248.
- 894 Passerat de Silans, A., 1986. Transferts de masse et de chaleur dans un  
895 sol stratifié soumis à une excitation atmosphérique naturelle. Comparai-  
896 son modèle expérience. PhD Thesis, Institut National Polytechnique de  
897 Grenoble, France.
- 898 Peng, J., Loew, A., Merlin, O., Verhoest, N. E., 2017. A review of spatial  
899 downscaling of satellite remotely sensed soil moisture. *Rev. of Geophys.*  
900 55 (2), 341–366.
- 901 Prévot, L., Bernard, R., Taconet, O., Madjar, D. V., 1984. Evaporation from  
902 a bare soil evaluated using a bare soil water transfer model and remotely  
903 sensed surface soil moisture data. *Water Resour. Res.* 20 (2), 311–316.

- 904 Schlesinger, W. H., Jasechko, S., 2014. Transpiration in the global water  
905 cycle. *Agr. For. Meteorol.* 189, 115–117.
- 906 Sellers, P. J., Heiser, M. D., Hall, F. G., 1992. Relations between surface  
907 conductance and spectral vegetation indices at intermediate ( $100 \text{ m}^2$  to  $15$   
908  $\text{km}^2$ ) length scales. *J. Geophys. Res.* 97 (D17), 19033–19059.
- 909 Shahraeeni, E., Lehmann, P., Or, D., 2012. Coupling of evaporative fluxes  
910 from drying porous surfaces with air boundary layer: Characteristics of  
911 evaporation from discrete pores. *Water Resour. Res.* 48, W09525.
- 912 Shuttleworth, W. J., Wallace, J. S., 1985. Evaporation from sparse canopies-  
913 an energy combination theory. *Q. J. R. Meteorol. Soc.* 111, 839–855.
- 914 Soarès, J., Bernard, R., Taconet, O., Vidal-Madjar, D., Weill., A., 1988. Es-  
915 timation of bare soil evaporation from airborne measurements. *J. Hydrol.*  
916 99, 281–296.
- 917 Stefan, V. G., Merlin, O., Er-Raki, S., Escorihuela, M.-J., Khabba, S., 2015.  
918 Consistency between in situ, model-derived and high-resolution-image-  
919 based soil temperature endmembers: Towards a robust data-based model  
920 for multi-resolution monitoring of crop evapotranspiration. *Remote Sens.*  
921 7 (8), 10444–10479.
- 922 Tuzet, A., Perrier, A., Leuning, R., 2003. A coupled model of stomatal con-  
923 ductance, photosynthesis and transpiration. *Plant, Cell & Environ.* 26 (7),  
924 1097–1116.

- 925 Van de Griend, A. A., Owe, M., 1994. Bare soil surface resistance to evap-  
926 oration by vapor diffusion under semiarid conditions. *Water Resour. Res.*  
927 30 (2), 181–188.
- 928 Wetzel, P. J., Chang, J.-T., 1988. Evapotranspiration from nonuniform sur-  
929 faces: a first approach for short-term numerical weather prediction. *Monthly*  
930 *Weather Rev.* 116, 600–621.
- 931 Yang, K., Koike, T., Ishikawa, H., Kim, J., Li, X., Liu, H., Liu, S., Ma, Y.,  
932 Wang, J., 2008. Turbulent flux transfer over bare-soil surfaces: character-  
933 istics and parameterization. *J. Appl. Meteorol. Clim.* 47 (1), 276–290.
- 934 Zhan, W., Chen, Y., Zhou, J., Wang, J., Liu, W., Voogt, J., Zhu, X., Quan,  
935 J., Li, J., 2013. Disaggregation of remotely sensed land surface temper-  
936 ature: Literature survey, taxonomy, issues, and caveats. *Remote Sens.*  
937 *Environ.* 131, 119–139.
- 938 Zhang, L., Dawes, W., Walker, G., 2001. Response of mean annual evap-  
939 otranspiration to vegetation changes at catchment scale. *Water Resour.*  
940 *Res.* 37 (3), 701–708.

Table 1: Start and end day of year (DOY) of the 9 study periods, including the whole bare soil period ( $P0$ ) at Sidi Rahal site in 2016 and its 8 subperiods ( $P1 - 8$ ) bounded by significant rainfall events. The soil moisture range, mean soil moisture, mean EC-derived SEE and mean potential evaporation are also listed for each period.

Period	Start (DOY)	End (DOY)	$\theta$ range (m <sup>3</sup> m <sup>-3</sup> )	mean $\theta$ (m <sup>3</sup> m <sup>-3</sup> )	mean $SEE_{EC}$ (-)	mean $LEp$ (Wm <sup>-2</sup> )
$P0$	1	243	0.03–0.38	0.06	0.24	354
$P1$	1	8	0.05–0.24	0.10	0.38	238
$P2$	9	45	0.04–0.23	0.08	0.33	242
$P3$	46	57	0.05–0.25	0.10	0.40	283
$P4$	58	80	0.05–0.33	0.10	0.32	286
$P5$	81	95	0.07–0.38	0.14	0.46	313
$P6$	96	125	0.04–0.22	0.07	0.27	342
$P7$	126	234	0.03–0.12	0.04	0.16	398
$P8$	235	243	0.03–0.16	0.05	0.20	386

Table 2: List of  $\theta_{1/2}$  and  $\Delta\theta_{1/2}^{-1}$  parameters retrieved from EC measurements for data with  $LEp > 100 \text{ Wm}^{-2}$  (for data with  $LEp > 400 \text{ Wm}^{-2}$  in parenthesis) and for periods  $P0-8$  separately.

Period	$\theta_{1/2}$ ( $\text{m}^3\text{m}^{-3}$ )	$\Delta\theta_{1/2}^{-1}$ ( $\text{m}^3\text{m}^{-3}$ )
$P0$	0.119 (0.129)	4.58 (4.01)
$P1$	0.129 (NA)	4.72 (NA)
$P2$	0.126 (NA)	4.54 (NA)
$P3$	0.112 (NA)	8.41 (NA)
$P4$	0.140 (NA)	5.61 (NA)
$P5$	0.156 (0.146)	4.49 (3.77)
$P6$	0.136 (0.136)	3.90 (3.51)
$P7$	0.073 (0.073)	11.0 (11.2)
$P8$	0.120 (0.120)	5.40 (5.22)

Table 3: Correlation coefficient (R), slope of the linear regression (S) and root mean square difference (RMSD) between modeled and EC-derived SEE for study periods  $P0 - 8$  separately. Model parameters are calibrated using EC measurements for data with  $LEp > 100 \text{ Wm}^{-2}$  during corresponding period  $P0 - 8$  (during period  $P0$  in parenthesis).

Period	R (-)			S (-)			RMSD (-)		
	PdS86	M16	New	PdS86	M16	New	PdS86	M16	New
$P0$	0.75 (0.75)	0.80 (0.80)	<b>0.85 (0.85)</b>	0.74 (0.74)	0.86 (0.86)	<b>0.91 (0.91)</b>	0.13 (0.13)	0.12 (0.12)	<b>0.10 (0.10)</b>
$P1$	0.94 (0.94)	0.94 (0.94)	<b>0.97 (0.97)</b>	0.82 (0.82)	0.85 (0.83)	<b>0.87 (0.85)</b>	0.11 (0.11)	0.11 (0.12)	<b>0.08 (0.08)</b>
$P2$	0.84 (0.84)	0.85 (0.84)	<b>0.92 (0.92)</b>	0.99 (0.99)	0.95 (0.95)	<b>1.01 (1.02)</b>	0.12 (0.12)	0.10 (0.11)	0.08 ( <b>0.07</b> )
$P3$	0.55 (0.55)	0.57 (0.55)	0.63 ( <b>0.64</b> )	0.57 (0.57)	0.89 (0.60)	<b>0.98 (0.70)</b>	0.21 (0.21)	0.25 (0.19)	0.24 ( <b>0.18</b> )
$P4$	0.64 (0.64)	0.66 (0.66)	0.72 ( <b>0.73</b> )	0.73 (0.73)	0.84 (0.74)	<b>0.88 (0.80)</b>	0.21 (0.21)	0.22 (0.22)	<b>0.19 (0.19)</b>
$P5$	0.78 (0.78)	0.85 (0.80)	<b>0.92 (0.88)</b>	0.82 (0.82)	0.95 (0.77)	<b>1.03 (0.86)</b>	0.19 (0.19)	0.15 (0.20)	<b>0.12 (0.16)</b>
$P6$	0.69 (0.69)	0.72 (0.70)	<b>0.84 (0.81)</b>	0.87 (0.87)	0.85 (0.96)	<b>1.01 (1.11)</b>	0.12 (0.12)	0.11 (0.13)	<b>0.09 (0.11)</b>
$P7$	0.30 (0.30)	0.79 (0.71)	<b>0.87 (0.77)</b>	0.12 (0.12)	0.80 (0.29)	<b>0.91 (0.41)</b>	0.10 (0.10)	0.07 (0.08)	<b>0.05 (0.07)</b>
$P8$	<b>0.85 (0.85)</b>	0.82 (0.82)	0.83 (0.83)	0.83 (0.83)	0.78 (0.71)	<b>0.89 (0.84)</b>	0.08 (0.08)	0.08 ( <b>0.07</b> )	0.08 (0.08)

Table 4: Correlation coefficient (R), slope of the linear regression (S) and root mean square difference (RMSD) between simulated and measured evaporation at Sidi Rahal site.

Model	R (-)	S (-)	RMSD ( $\text{Wm}^{-2}$ )
PdS86	0.81	0.89	34
M16	0.83	0.96	35
New	0.85	0.96	32

Table 5: Same as for Table 2 with model parameters calibrated using TI measurements.

Period	$\theta_{1/2}$ ( $\text{m}^3\text{m}^{-3}$ )	$\Delta\theta_{1/2}^{-1}$ ( $\text{m}^3\text{m}^{-3}$ )
<i>P0</i>	0.085 (0.125)	10.0 (4.21)
<i>P1</i>	0.086 (NA)	9.31 (NA)
<i>P2</i>	0.086 (NA)	12.7 (NA)
<i>P3</i>	0.093 (NA)	23.3 (NA)
<i>P4</i>	0.108 (0.128)	10.1 (5.63)
<i>P5</i>	0.143 (0.164)	9.86 (3.95)
<i>P6</i>	0.102 (0.150)	10.5 (3.52)
<i>P7</i>	0.055 (0.063)	20.1 (19.9)
<i>P8</i>	0.080 (0.111)	17.7 (6.46)

Table 6: Same as for Table 3 with model parameters calibrated using TI measurements for data with  $LEp > 100 \text{ Wm}^{-2}$  during corresponding period  $P0 - 8$  (for data with  $LEp > 400 \text{ Wm}^{-2}$  during period  $P0$  in parenthesis).

Period	R (-)			S (-)			RMSD (-)		
	PdS86	M16	New	PdS86	M16	New	PdS86	M16	New
$P0$	0.77 (0.75)	0.77 (0.80)	0.81 ( <b>0.86</b> )	1.15 (0.71)	1.23 (0.82)	1.25 ( <b>0.87</b> )	0.18 (0.13)	0.19 (0.11)	0.17 ( <b>0.10</b> )
$P1$	0.89 (0.94)	0.89 (0.94)	0.92 ( <b>0.98</b> )	<b>1.02</b> (0.81)	0.96 (0.79)	0.97 (0.82)	0.20 (0.11)	0.21 (0.11)	0.17 ( <b>0.08</b> )
$P2$	0.81 (0.86)	0.77 (0.85)	0.82 ( <b>0.94</b> )	1.32 (1.02)	1.36 (0.90)	1.42 ( <b>0.98</b> )	0.20 (0.12)	0.22 (0.10)	0.19 ( <b>0.07</b> )
$P3$	0.43 (0.26)	0.48 (0.55)	0.52 ( <b>0.65</b> )	0.71 (0.31)	<b>1.04</b> (0.56)	1.08 (0.68)	0.32 (0.28)	0.37 (0.19)	0.35 ( <b>0.17</b> )
$P4$	0.68 ( <b>0.82</b> )	0.63 (0.65)	0.67 (0.74)	<b>1.01</b> (0.82)	1.02 (0.70)	1.03 (0.77)	0.28 ( <b>0.14</b> )	0.29 (0.21)	0.26 (0.18)
$P5$	0.60 (0.72)	0.77 (0.81)	0.82 ( <b>0.90</b> )	0.55 (0.76)	1.17 (0.78)	1.21 ( <b>0.89</b> )	0.35 (0.20)	0.25 (0.18)	0.22 ( <b>0.14</b> )
$P6$	0.60 (0.70)	0.64 (0.71)	0.70 ( <b>0.83</b> )	1.22 (0.85)	1.36 (0.91)	1.44 ( <b>1.09</b> )	0.22 (0.12)	0.22 (0.12)	0.21 ( <b>0.10</b> )
$P7$	0.77 (0.40)	0.76 (0.70)	<b>0.82</b> (0.69)	0.52 (0.15)	<b>1.24</b> (0.26)	1.37 (0.42)	0.08 (0.10)	0.12 (0.08)	0.12 ( <b>0.07</b> )
$P8$	<b>0.87</b> (0.85)	0.84 (0.81)	0.86 (0.79)	1.55 (0.78)	1.85 (0.64)	1.85 ( <b>0.80</b> )	0.13 (0.07)	0.19 ( <b>0.07</b> )	0.18 (0.08)

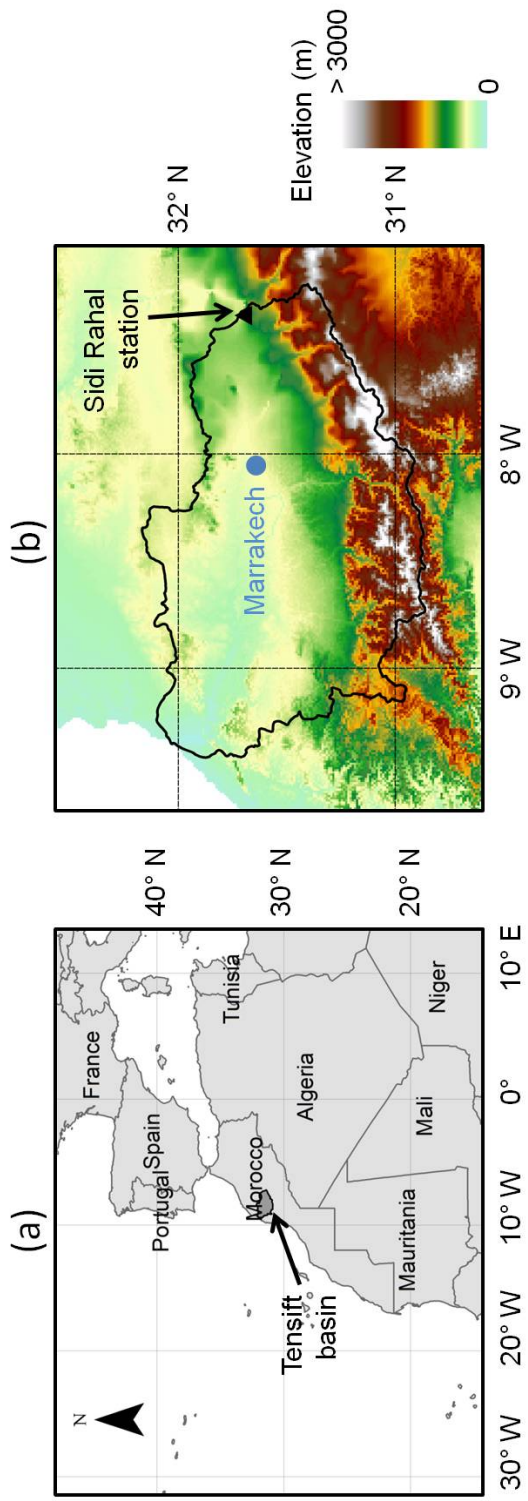


Figure 1: Geographic location of the Tensift basin in Morocco (a) and the Sidi Rahal flux site within the catchment (b).

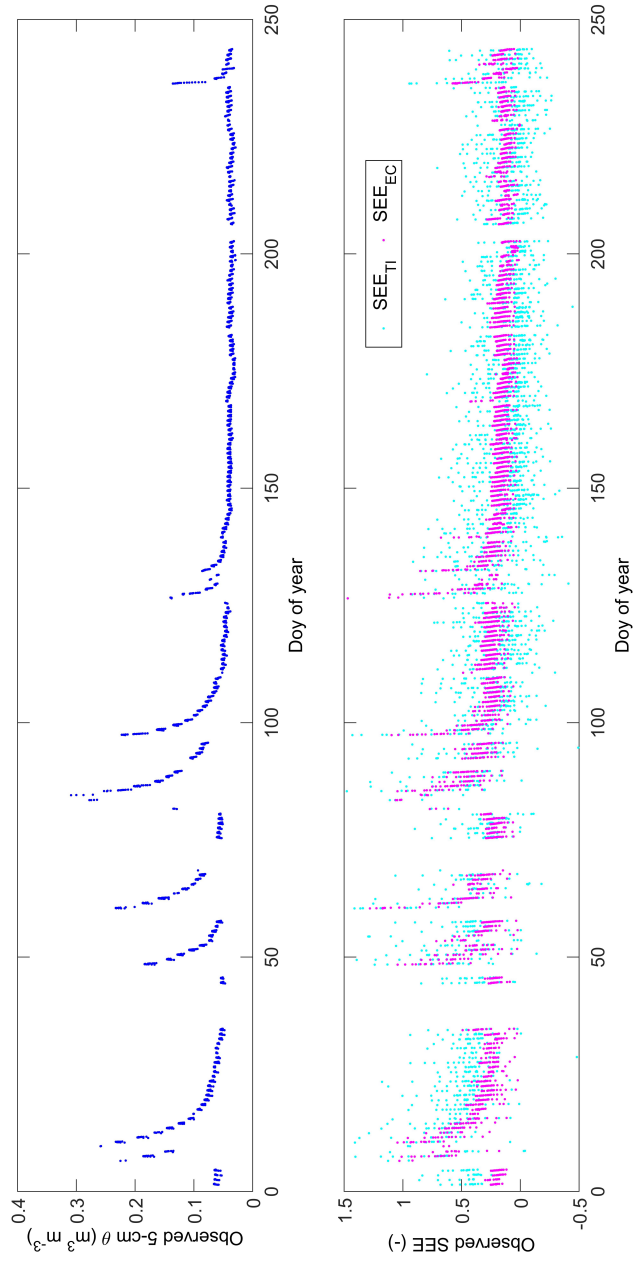


Figure 2: Time series of near surface soil moisture ( $\theta$ ) and EC-derived ( $SEE_{EC}$ ) and TI-derived ( $SEE_{TI}$ ) SEE in 2016 at the Sidi Rahal site.

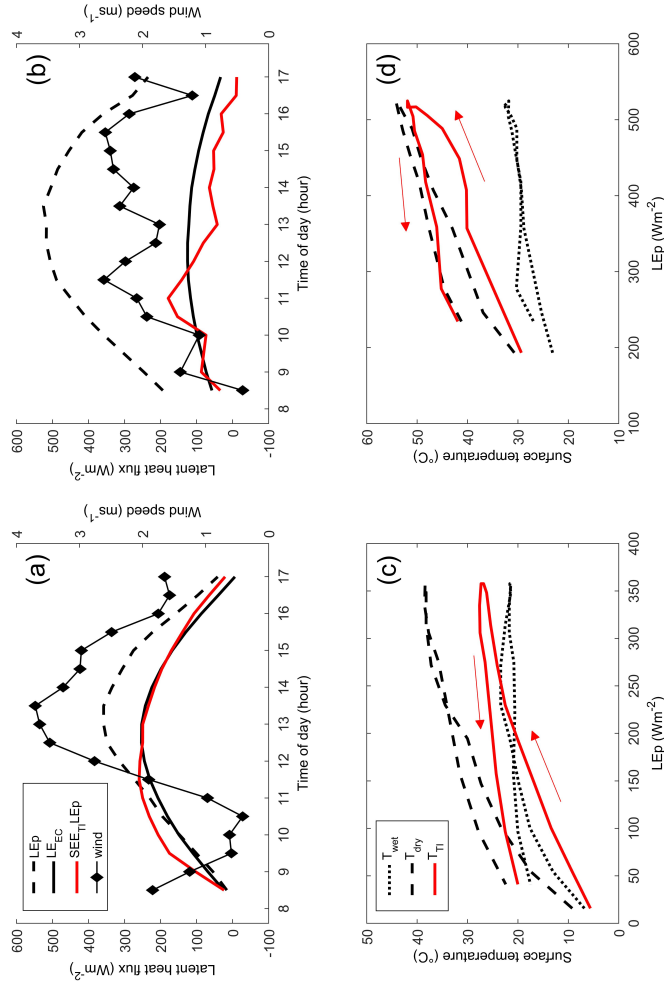


Figure 3: Variations between 8:30 am and 5:00 pm of the potential soil evaporation ( $LE_p$ ), the soil evaporation measured by the EC ( $LE_{EC}$ ), the soil evaporation estimated as the TI-derived SEE ( $SEE_{TI}$ ) times  $LE_p$  and wind speed in relatively wet (a) and dry (b) conditions, on January 7th and May 1st 2016 respectively. The hysteretic behavior of radiometric temperature is also shown as a function of  $LE_p$  on the wet (c) and dry (d) date, respectively.

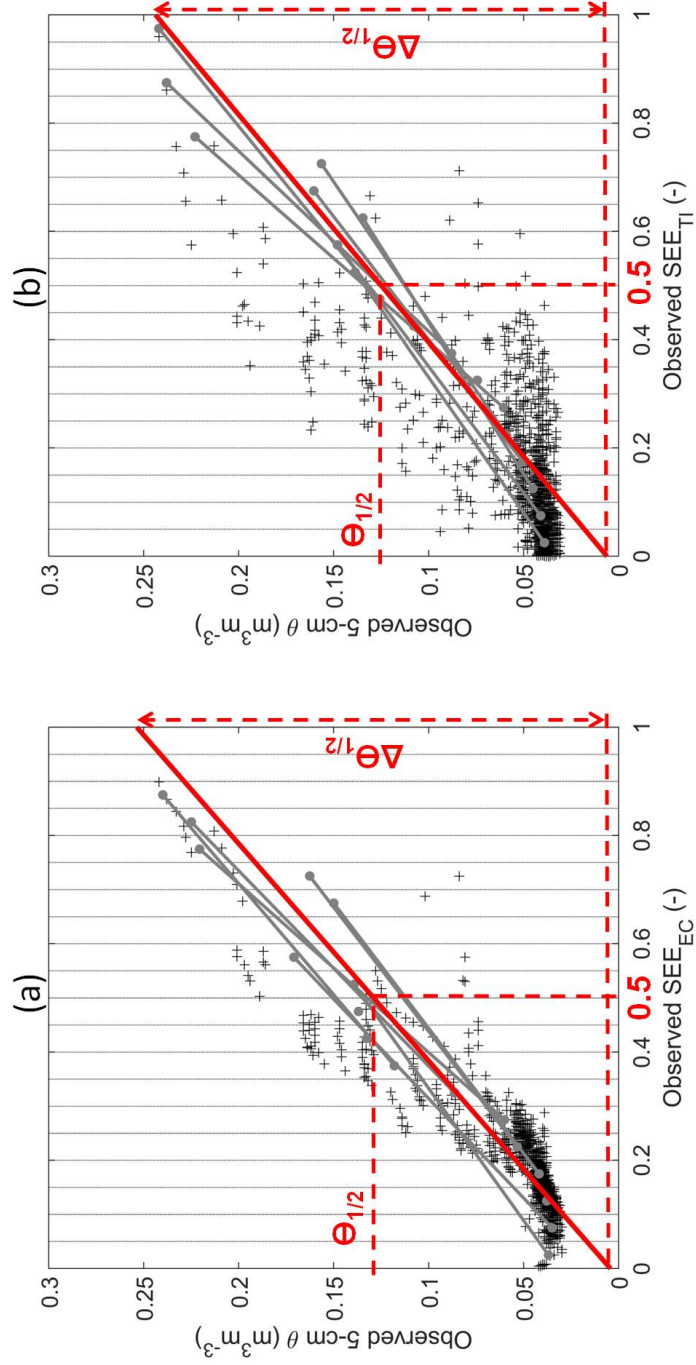


Figure 4: Retrieval of the pair  $(\theta_{1/2}, \Delta\theta_{1/2}^{-1})$  during period  $P0$  for data with  $LEp > 400 \text{ W m}^{-2}$  and for EC-derived (a) and TI-derived (b) SEE separately.

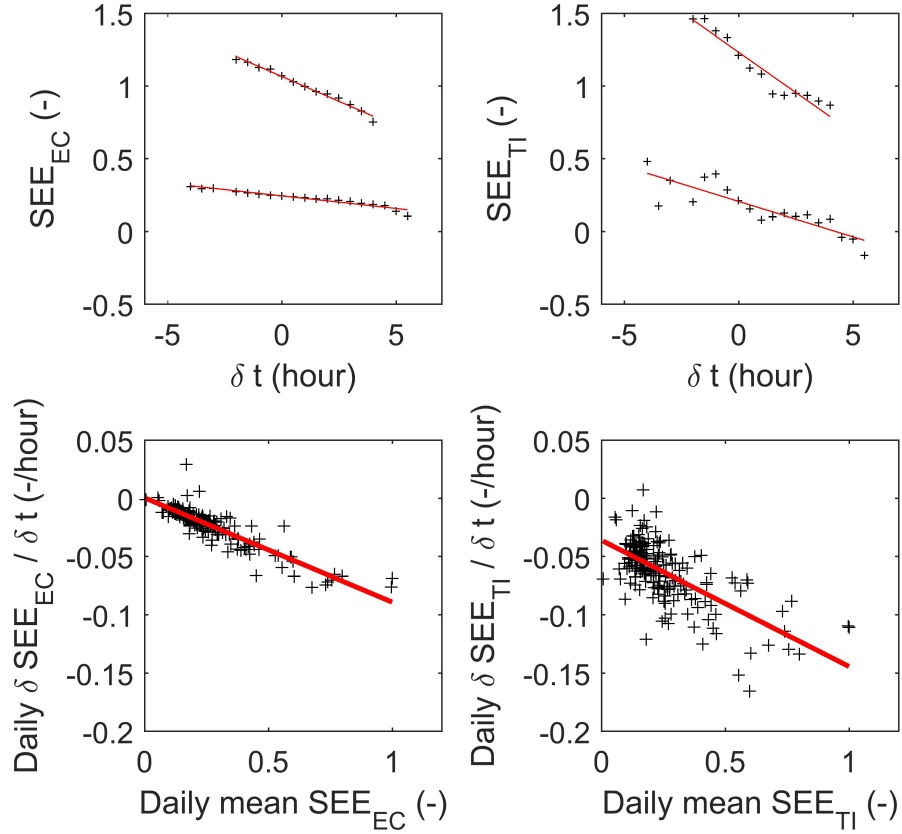


Figure 5: The observed SEE for data with  $LEp > 100 \text{ Wm}^{-2}$  is plotted as a function of  $\delta t$  at the daily time scale for a wet (January 7th) and dry (May 1st 2016) day (top) and the estimated daily slope  $\delta SEE / \delta t$  is plotted as a function of the daily mean SEE (bottom) for each day of period  $P0$  and for the EC-derived (left) and TI-derived (right) SEE case separately.

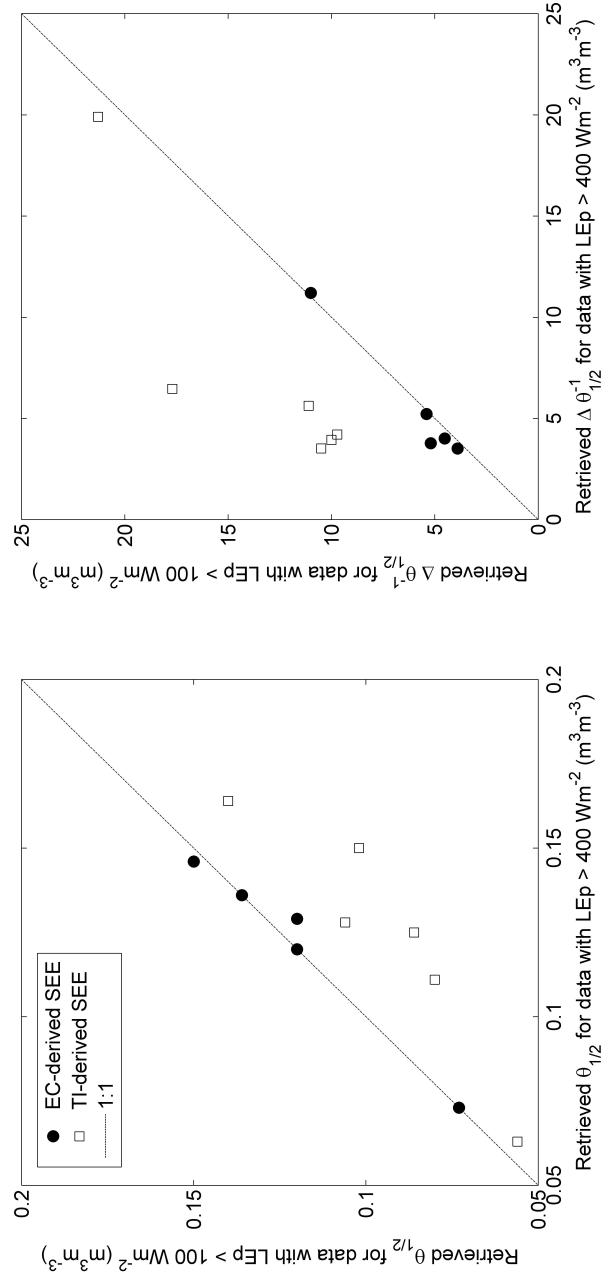


Figure 6: Retrieved  $\theta_{1/2}$  (left) and retrieved  $\Delta\theta_{1/2}^{-1}$  (right) for data with  $LEp > 100 \text{ Wm}^{-2}$  versus the same parameter retrieved for data with  $LEp > 400 \text{ Wm}^{-2}$ .

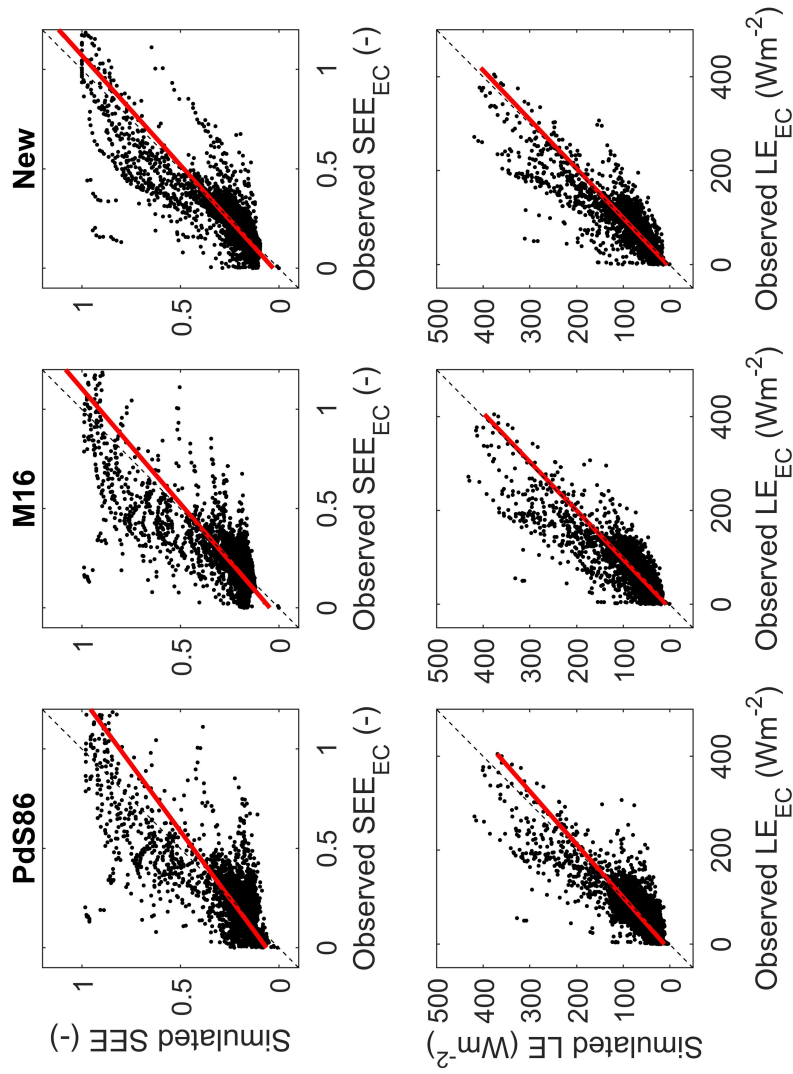


Figure 7: Simulated versus observed (EC-derived) SEE (top) and evaporation (bottom) for  $P0$  data with  $LEp > 100 \text{ W m}^{-2}$  and for three (PdS86, M16 and new)  $\tau_{ss}$  models separately. In all three cases, both  $\theta_{1/2}$  and  $\Delta\theta_{1/2}^{-1}$  are calibrated during  $P0$  from EC-derived SEE data with  $LEp > 100 \text{ W m}^{-2}$ .

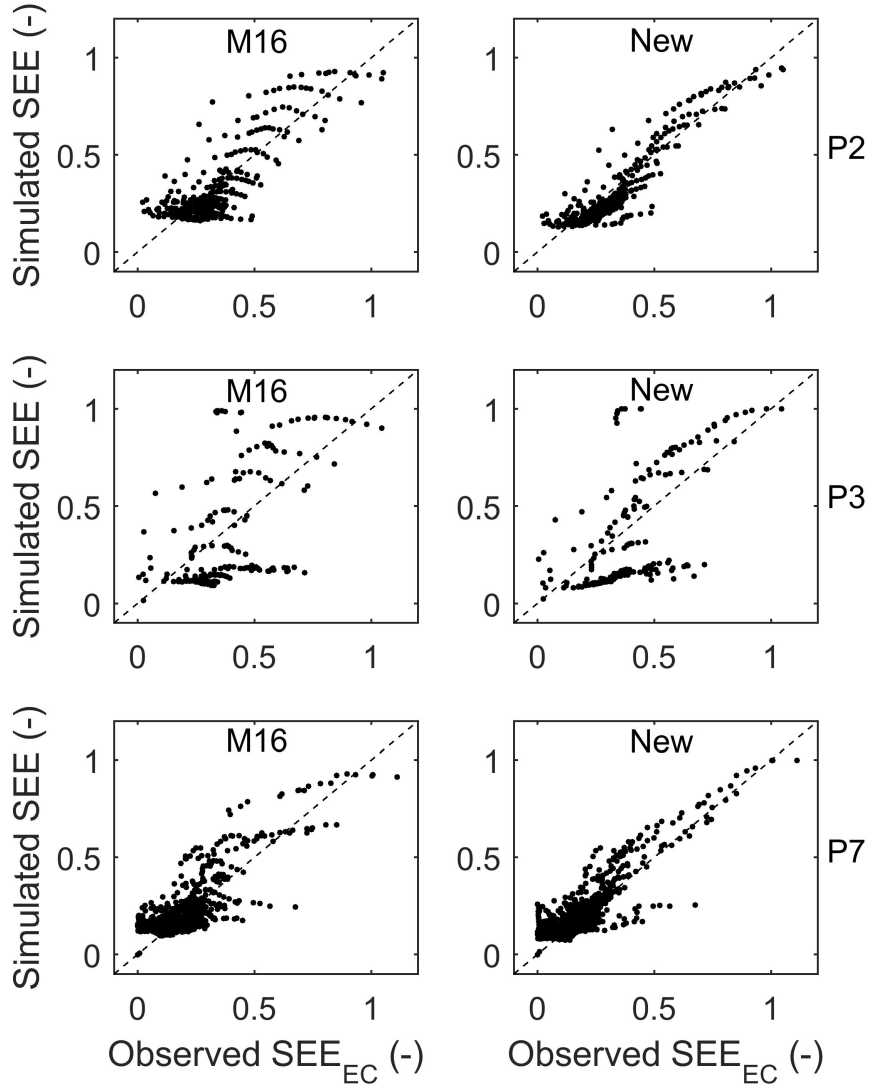


Figure 8: Simulated versus observed (EC-derived) SEE for data with  $LEp > 100 \text{ W m}^{-2}$  during P2 (top), P3 (middle) and P7 (bottom) period and for M16 and new models separately. In all six cases, both  $\theta_{1/2}$  and  $\Delta\theta_{1/2}^{-1}$  are calibrated during  $P0$  from EC-derived SEE data with  $LEp > 100 \text{ W m}^{-2}$ .

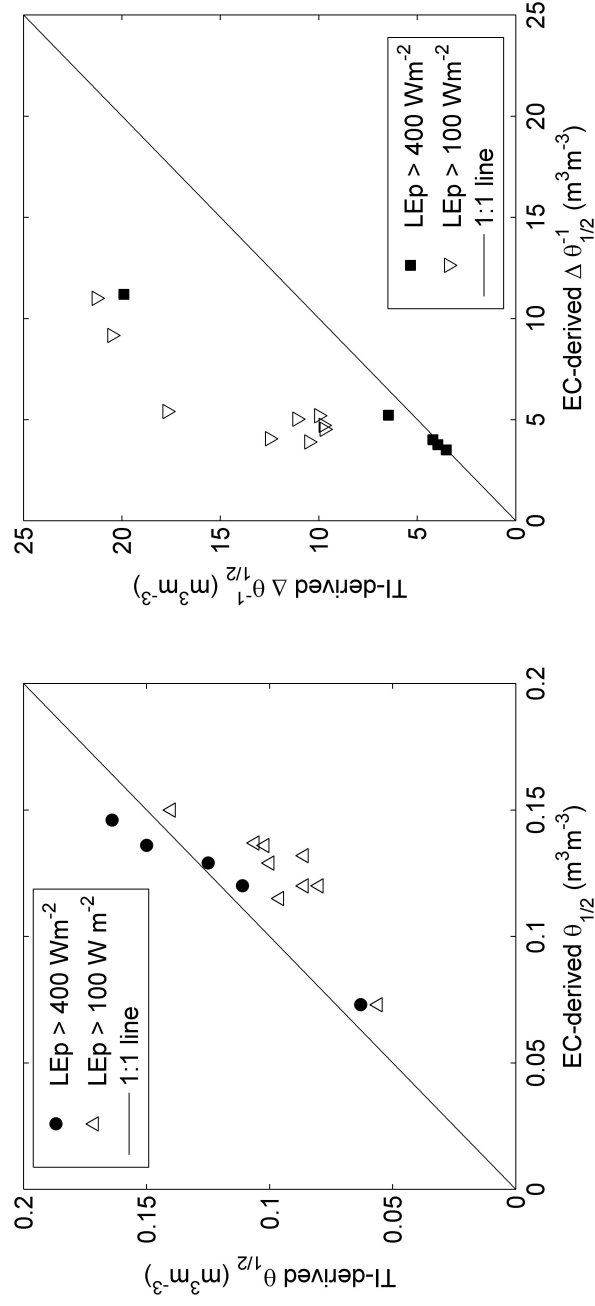


Figure 9: TI-derived versus EC-derived  $\theta_{1/2}$  (left) and TI-derived versus EC-derived  $\Delta\theta_{1/2}^{-1}$  (right) for data with a minimum  $LEp$  value of 100 and  $400 \text{ Wm}^{-2}$  separately.

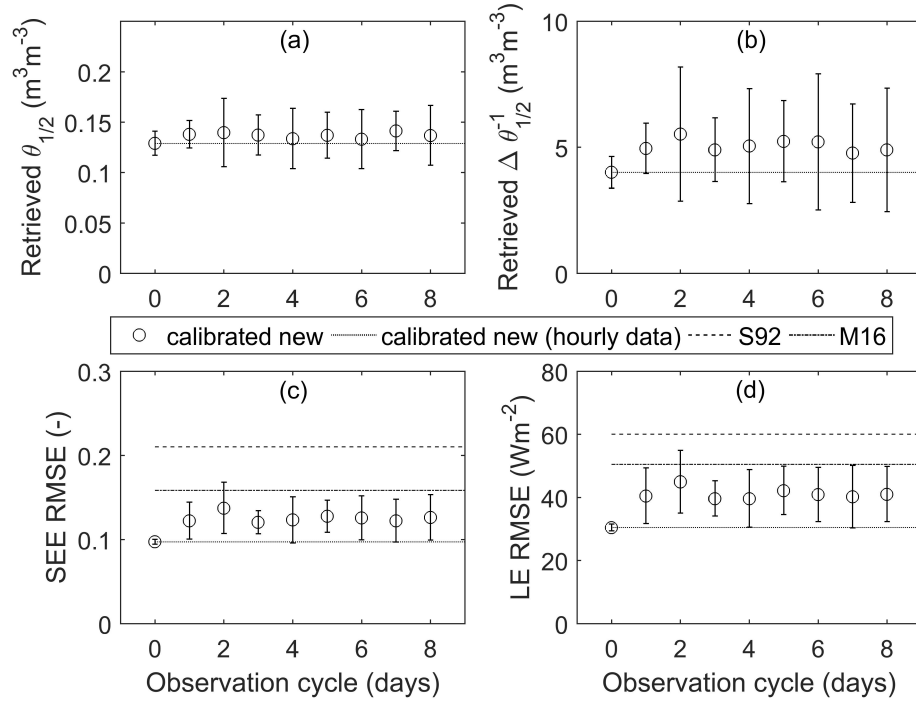


Figure 10: Model results in terms of (a) retrieved  $\theta_{1/2}$ , (b) retrieved  $\Delta\theta_{1/2}^{-1}$ , (c) RMSE in simulated SEE and (d) RMSE in simulated evaporation are presented for an increasing observation cycle –ranging from the hourly to the 8-day period– of TI calibration data. The mean (circles) and standard deviation (errorbars) of retrieved parameters are computed from an ensemble of input TI data sets (with  $LEp > 400 \text{ Wm}^{-2}$ ) collected at 11:30 am, 12:00pm and 12:30pm separately and, for observation cycles longer than 1 day, on all possible observation cycles shifted by 1 day. The mean (circles) and standard deviation (errorbars) of RMSE in SEE/LE are computed from data (with  $LEp > 100 \text{ Wm}^{-2}$ ) during the whole study period using the ensemble of parameter pairs  $(\theta_{1/2}, \Delta\theta_{1/2}^{-1})$  retrieved previously. For comparison purposes, the RMSE of the SEE/LE estimated by M16 (pedotransfer function) and S92 (fixed parameters) is also plotted.